arXiv:1207.3817v2 [cond-mat.quant-gas] 27 Sep 2012

Mean-field dynamics of two-mode Bose-Einstein condensates in highly anisotropic potentials: Interference, dimensionality, and entanglement

Alexandre B. Tacla

Center for Quantum Information and Control, MSC07–4220, University of New Mexico, Albuquerque, New Mexico 87131-0001, USA

E-mail: `tacla@unm.edu`

Carlton M. Caves

Center for Quantum Information and Control, MSC07–4220, University of New Mexico, Albuquerque, New Mexico 87131-0001, USA
Centre for Engineered Quantum Systems, School of Mathematics and Physics, University of Queensland, Brisbane, Queensland 4072, Australia

Abstract. We study the mean-field dynamics and the reduced-dimension character of two-mode Bose-Einstein condensates (BECs) in highly anisotropic traps. By means of perturbative techniques, we show that the tightly confined (transverse) degrees of freedom can be decoupled from the dynamical equations at the expense of introducing additional effective three-body, attractive, intra- and inter-mode interactions into the dynamics of the loosely confined (longitudinal) degrees of freedom. These effective interactions are mediated by changes in the transverse wave function. The perturbation theory is valid as long as the nonlinear scattering energy is small compared to the transverse energy scales. This approach leads to reduced-dimension mean-field equations that optimally describe the evolution of a two-mode condensate in general quasi-1D and quasi-2D geometries. We use this model to investigate the relative phase and density dynamics of a two-mode, cigar-shaped ^{87}Rb BEC. We study the relative-phase dynamics in the context of a nonlinear Ramsey interferometry scheme, which has recently been proposed as a novel platform for high-precision interferometry. Numerical integration of the coupled, time-dependent, three-dimensional, two-mode Gross-Pitaevskii equations for various atom numbers shows that this model gives a considerably more refined analytical account of the mean-field evolution than an idealized quasi-1D description.

Contents

1 Introduction 2

2 Two-mode dynamics in the reduced-dimension approximation 4

3 Two-mode dynamics via the relative-state decomposition 5

4 Adiabatic elimination of φ_n^α 11
4.1 Single-mode dynamics within the adiabatic elimination of φ_n^α 14

5 Two-mode dynamics of a cigar-shaped ^{87}Rb condensate 15
5.1 Two-mode evolution 15
5.2 Numerical simulations 17
5.3 Differential phase dynamics: nonlinear Ramsey interferometry 18
5.4 Time scales 19
5.4.1 Ramsey fringes. 20
5.4.2 Source terms. 23
5.4.3 Thomas-Fermi estimates. 25
5.5 Average densities 28

6 Optimal reduced-dimension equations for the two-mode evolution 37

7 Conclusion 44

1. Introduction

Quantum protocols for nonlinear interferometry using two-mode Bose-Einstein condensates (BECs) have recently been proposed as a novel platform for weak-signal detection [1, 2, 3]. More specifically, a two-mode ^{87}Rb BEC consisting of N atoms can be used to implement a nonlinear Ramsey interferometer that potentially operates near the limits established by quantum mechanics [4, 5, 6]. This protocol is able to achieve detection sensitivities that scale better than the optimal $1/N$ limit of linear interferometry [7], without relying on complicated state preparation or measurement procedures nor on entanglement generation to enhance the measurement sensitivity [2]. For these reasons, this scheme can be particularly attractive from an experimental perspective.

As discussed in previous work [4, 5, 6], there are several conditions for observing nonlinearity-enhanced scalings in this system. For instance, the expansion of the condensate with increasing atom number can get in the way of achieving the desired scaling, as it essentially dilutes the nonlinear interactions in the condensate. Although this effect can be completely suppressed by hard-walled homogeneous potentials, confining the condensate in highly anisotropic traps is a more realistic solution. In this way, the expansion of the atomic cloud in the tightly confined directions is effectively suppressed, with highly elongated geometries providing the architecture with best scalings.

In view of currently available techniques and typical experimental parameters, we numerically simulated such a nonlinear BEC interferometer in cigar-shaped (quasi-1D) potentials [5]. Interestingly, our simulations revealed that the interferometer's signal can be sensitive to the three-dimensional nature of the condensate. In spite of the highly elongated confinement, we found significant deviations from a quasi-1D model as the strength of the nonlinear scattering interaction increases. In this reduced-dimension approximation, it is assumed that the tightly confined (transverse) dimensions can be effectively neglected on the grounds that the characteristic transverse energy scale far exceeds the scattering interaction energy of the atomic cloud. In this situation, however, there are still position-dependent phase shifts that need to be modeled precisely for an accurate analytical description of the interferometry process. This brings into question the accuracy of the reduced-dimension approximation, both spatially and temporally.

To better model the ground-state properties of a BEC in highly anisotropic potentials, we derived corrections to such approximation by means of perturbative techniques [8]. Using a perspective borrowed from quantum information theory, we developed a perturbative Schmidt decomposition of the condensate wave function between the transverse direction(s) and the loosely confined (longitudinal) direction(s). This formalism provides corrections to the lowest-order transverse and longitudinal wave functions of the reduced-dimension approximation; the main effect is a reshaping of the BEC in the tightly confined direction(s) as the strength of the nonlinear scattering interaction increases. In addition, because the perturbation formalism is tied to the Schmidt decomposition, it automatically encodes information about the entanglement between the spatial directions in higher-order Schmidt terms; the leading Schmidt term provides the optimal product approximation to the exact three-dimensional ground-state mean-field solution.

In this article, we develop further the approach of Ref. [8] by extending our perturbation theory to the mean-field dynamics of two-mode BECs in highly anisotropic traps. The perturbation theory is valid as long as the nonlinear scattering energy is small compared to the transverse energy scales. This approach leads to equations that effectively describe the evolution of a two-mode condensate in general quasi-1D and quasi-2D geometries. In addition, we also derive effective time-evolution equations for a highly anisotropic, single-mode BEC. These equations show how the corrections to the reduced-dimension approximation propagate in time and affect the overall dynamics of the condensate, thus modeling not only interference effects, but also density dynamics. We apply this 3D-corrected model to analyze the nonlinear BEC interferometry protocol simulated in [5] for cigar-shaped potentials. This analysis leads to a considerably more refined analytical account of the interference signal than the one given by a quasi-1D model. In addition, we study the spatial segregation of the two modes, which occurs on a longer timescale than the phase accumulation. We compare this model against exact three-dimensional numerical results for the evolution of the two-mode BEC given by the three-dimensional, two-mode, coupled Gross-Pitaevskii equations. Finally, we investigate the reduced-dimension structure of the highly anisotropic, two-mode condensate by explicitly deriving the instantaneous Schmidt decomposition of the time-dependent, two-mode condensate state. This analysis allows us to study the entanglement between the transverse and the longitudinal-internal degrees of freedom. It confirms that the tightly confined dimensions can indeed be decoupled from the evolution equation and naturally shows the optimal way to do it.

This article is organized as follows. In Sec. 2, we briefly recount the reduced-dimension approximation to the three-dimensional, two-mode, coupled Gross-Pitaevskii equations, which completely neglects the effect of the nonlinear scattering interaction on the transverse degrees of freedom. By developing a perturbative relative-state decomposition of the time-dependent condensate mean fields, we derive corrections to this approximation in Sec. 3; these corrections act as effective three-body, attractive, intra- and inter-mode interactions. Because of the high anisotropy of the condensate, the evolution of the longitudinal modes in the perturbative regime takes place on a much longer time scale than the transverse modes. We address this separation of times scales in Sec. 4 and derive an adiabatic approximation to the longitudinal evolution equations of Sec. 3. In Sec. 5, we use this model to investigate the relative-phase and density dynamics of a two-mode, cigar-shaped ^{87}Rb BEC. We study the relative-phase dynamics in the context of a nonlinear Ramsey interferometry scheme. We compare our perturbative model against numerical integration of the full three-dimensional two-mode, coupled Gross-Pitaevskii equations for various atom numbers. Lastly, in Sec. 6, we investigate the reduced-dimension character of the two-mode condensate by explicitly deriving the instantaneous Schmidt decomposition of the time-dependent, two-mode condensate singe-particle state. Conclusions are given in Sec.7.

2. Two-mode dynamics in the reduced-dimension approximation

In the mean-field approximation, one describes the evolution of a two-mode condensate at zero temperature by unity-normalized wave functions $\psi^1(\mathbf{r},t)$ and $\psi^2(\mathbf{r},t)$ for the two modes, which are determined by the two-mode, coupled, time-dependent, three-dimensional Gross-Pitaevskii (GP) equations

$$i\hbar\frac{\partial\psi^\alpha}{\partial t}=\Big(-\frac{\hbar^2}{2m}\nabla^2+V+g_{\alpha\alpha}(N_\alpha-1)|\psi^\alpha|^2+g_{\alpha\beta}(N_\beta-1)|\psi^\beta|^2\Big)\psi^\alpha. \tag{1}$$

Here $N_{1(2)}$ is the number of atoms in mode 1 (2), V is the external trapping potential, assumed to be the same for both modes, and $\alpha=1,2$ and $\beta=2,1$ label the two modes of the condensate, which can represent, for instance, two hyperfine states, $|1\rangle$

and $|2\rangle$. We further assume that collisions between the atoms are elastic, so that the only allowed scattering processes are $|1\rangle|1\rangle \rightarrow |1\rangle|1\rangle$, $|2\rangle|2\rangle \rightarrow |2\rangle|2\rangle$, and $|1\rangle|2\rangle \rightarrow |1\rangle|2\rangle$, with scattering strengths g_{11}, g_{22}, and g_{12}, where $g_{\alpha\beta} = 4\pi\hbar^2 a_{\alpha\beta}/m$ is determined by the s-wave scattering length $a_{\alpha\beta}$ and the atomic mass m. Note that by setting the inter-mode coupling constant g_{12} to zero, one recovers the case of a single-mode BEC, which we address in more detail in Sec. 4.1.

In the case of highly anisotropic potentials, the condensate is loosely trapped by a potential $V_L(\boldsymbol{r})$ in d dimensions, referred to as longitudinal (L) dimensions, as opposed to the remaining $D = 3 - d$ transverse degrees of freedom (T), which are tightly confined in a potential $V_T(\boldsymbol{\rho})$. If the scattering interaction is sufficiently small compared to the transverse energy scale, one can neglect the effect of the nonlinear interaction on the atomic transverse degrees of freedom and hence approximate the condensate wave functions by the product ansatz

$$\psi^{\alpha}_{\mathrm{rda}}(\boldsymbol{\rho}, \boldsymbol{r}, t) = e^{-iE_0 t/\hbar} \xi_0(\boldsymbol{\rho}) \phi^{\alpha}(\boldsymbol{r}, t), \tag{2}$$

where E_0 and $\xi_0(\boldsymbol{\rho})$ are, respectively, the ground-state energy and wave function of the bare transverse potential, $V_T(\boldsymbol{\rho})$. The longitudinal wave functions $\phi^{\alpha}(\boldsymbol{r}, t)$ are the solutions of the d-dimensional, longitudinal GP equations,

$$i\hbar \frac{\partial \phi^{\alpha}}{\partial t} = \left(-\frac{\hbar^2}{2m} \nabla_L^2 + V_L + g_{\alpha\alpha} \eta_T (N_\alpha - 1) |\phi^{\alpha}|^2 + g_{\alpha\beta} \eta_T (N_\beta - 1) |\phi^{\beta}|^2 \right) \phi^{\alpha}, \tag{3}$$

which are found by plugging Eq. (2) into the two-mode GP equations (1) and projecting the result onto the subspace spanned by ξ_0. Note that in this reduced-dimension picture, the coupling constants are renormalized by the average inverse transverse cross section of the condensate, given by

$$\eta_T = \int d^D\rho \, |\xi_0(\boldsymbol{\rho})|^4. \tag{4}$$

Within this approximation, the transverse and longitudinal degrees of freedom are decoupled. This approximation is only meaningful if the number of atoms in the condensate is small compared to an (upper) critical atom number $\mathcal{N}_T$, defined as the number at which the nonlinear scattering energies become comparable to the transverse kinetic energy. As N approaches $\mathcal{N}_T$, one can no longer neglect the effects of the scattering interaction on the condensate transverse degrees of freedom; as a result, the product ansatz (2) is no longer a good approximation to the 3D wave function. Such 3D-induced effects are responsible not only for modifying the transverse and longitudinal wave functions, but also for creating correlations between the spatial directions. All these effects can be readily calculated in the perturbative regime where N is small compared to $\mathcal{N}_T$.

3. Two-mode dynamics via the relative-state decomposition

In previous work [8], we found perturbative corrections to the reduced-dimension approximation for the ground-state wave function of a single-mode condensate. These corrections arise from the derivation of the Schmidt decomposition of the condensate wave function between the transverse and longitudinal degrees of freedom. To first-order this approach is equivalent to a first-order perturbative relative-state decomposition of the condensate wave function. The crucial difference between these two approaches is that the Schmidt decomposition assumes no prior knowledge of the basis elements used in the perturbation expansion, whereas in the relative-state method, the expansion is carried out relative to a fixed basis for the transverse degrees of freedom. For this reason, the expansion of the time-independent condensate wave function can be implemented in a simpler way if derived via the relative-state method rather than via the Schmidt decomposition. This motivates us to investigate the dynamics of the condensate from a similar perspective and to look for the perturbative relative-state decomposition of the time-dependent condensate mean field. We return to the Schmidt decomposition in Sec. 6 and show that a Schmidt decomposition of the three-dimensional, time-dependent mean-field solution can easily be retrieved from the relative-state decomposition.

As before, we model the two-mode dynamics of the condensate by means of the mean-field approximation, according to which the mean field of each BEC mode satisfies the time-dependent, coupled, two-mode Gross-Pitaevskii equation (1), which we write here as

$$i\hbar\dot{\psi}^{\alpha} = \Big(H_T + \epsilon H_L + \epsilon\tilde{g}_{\alpha\alpha}|\psi^{\alpha}|^2 + \epsilon\tilde{g}_{\alpha\beta}|\psi^{\beta}|^2\Big)\psi^{\alpha}. \tag{5}$$

For simplicity of notation, we now use $\dot{\psi}^{\alpha} = \partial\psi^{\alpha}/\partial t$, $\tilde{g}_{\alpha\alpha} = (N_{\alpha} - 1)g_{\alpha\alpha}$, and $\tilde{g}_{\alpha\beta} = (N_{\beta}-1)g_{\alpha\beta}$. Here $H_{T(L)} = -(\hbar^2/2m)\nabla^2_{T(L)} + V_{T(L)}$ is the transverse (longitudinal) single-particle Hamiltonian, and ϵ is a formal perturbation parameter that is set equal to 1 at the end of the calculation.

In the perturbative regime, we write the relative-state decomposition of the time-dependent condensate wave functions ψ^{α} as

$$\psi^{\alpha}(\boldsymbol{\rho},\boldsymbol{r},t) = \xi_0(\boldsymbol{\rho})\varphi_0^{\alpha}(\boldsymbol{r},t) + \epsilon\sum_{n=1}^{\infty}\xi_n(\boldsymbol{\rho})\varphi_n^{\alpha}(\boldsymbol{r},t), \tag{6}$$

where $\{\xi_n\}$ is the eigenbasis of the transverse Hamiltonian. The longitudinal wave functions φ_n^{α} are defined by the projection of the time-dependent mean-field solution ψ^{α} onto the transverse eigenfunctions ξ_n.

Before we carry out the perturbative expansion of the time-dependent, two-mode GP equations, it is convenient to redefine the longitudinal wave functions relative to an interaction picture in which fast, trivial oscillations are removed. Because of the high anisotropy of the trapping potential, we expect the transverse bare trap energy to be the fastest time scale in the perturbative regime, and therefore we define

$$\upphi_n^{\alpha}(t) \equiv e^{iE_0t/\hbar}\varphi_n^{\alpha}(t). \tag{7}$$

Now we expand the two-mode GP equations (5) to second order in powers of ϵ and project the result onto ξ_0, thus obtaining the following equation for φ_0^α:

$$\begin{aligned} i\hbar\dot{\varphi}_0^\alpha = {} & \epsilon \left(H_L + \tilde{g}_{\alpha\alpha}\eta_T|\varphi_0^\alpha|^2 + \tilde{g}_{\alpha\beta}\eta_T|\varphi_0^\beta|^2 \right) \varphi_0^\alpha \\ & + \epsilon^2 \sum_{n=1}^{\infty} \langle \xi_0^3|\xi_n\rangle \Big[\left(2\tilde{g}_{\alpha\alpha}|\varphi_0^\alpha|^2 + \tilde{g}_{\alpha\beta}|\varphi_0^\beta|^2 \right) \varphi_n^\alpha + \tilde{g}_{\alpha\alpha}(\varphi_0^\alpha)^2 \varphi_n^{\alpha *} \Big] \\ & + \epsilon^2 \tilde{g}_{\alpha\beta}\varphi_0^\alpha \sum_{n=1}^{\infty} \langle \xi_0^3|\xi_n\rangle \left(\varphi_0^\beta \varphi_n^{\beta *} + \varphi_0^{\beta *}\varphi_n^\beta \right). \end{aligned} \tag{8}$$

Hereafter, for brevity, we represent spatial integrals in terms of bra-ket inner products.

Similarly, the projection of Eq. (5) onto ξ_n, $n \geq 1$, yields to lowest order in ϵ the time-evolution equations for the longitudinal functions φ_n^α, which read

$$i\hbar\dot{\varphi}_n^\alpha = (E_n - E_0)\varphi_n^\alpha + \langle \xi_n|\xi_0^3\rangle \left(\tilde{g}_{\alpha\alpha}|\varphi_0^\alpha|^2 + \tilde{g}_{\alpha\beta}|\varphi_0^\beta|^2 \right) \varphi_0^\alpha + O(\epsilon), \quad n \geq 1. \tag{9}$$

One can integrate Eq. (9), obtaining the formal solution

$$\begin{aligned} & \varphi_n^\alpha(t) - \varphi_n^\alpha(0) e^{-i(E_n - E_0)t/\hbar} \\ & \quad = -\frac{i}{\hbar} \langle \xi_n|\xi_0^3\rangle \int_0^t ds\, e^{-i(E_n-E_0)(t-s)/\hbar} \Big(\tilde{g}_{\alpha\alpha}|\varphi_0^\alpha(s)|^2 + \tilde{g}_{\alpha\beta}|\varphi_0^\beta(s)|^2 \Big) \varphi_0^\alpha(s) + O(\epsilon). \end{aligned} \tag{10}$$

By plugging Eq. (10) back into Eq. (8), we eliminate $\varphi_n^\alpha(t)$ from the equation and get

$$\begin{aligned} i\hbar\dot{\varphi}_0^\alpha = {} & \epsilon \left(H_L + \tilde{g}_{\alpha\alpha}\eta_T|\varphi_0^\alpha|^2 + \tilde{g}_{\alpha\beta}\eta_T|\varphi_0^\beta|^2 \right) \varphi_0^\alpha \\ & + \epsilon^2 \eta_T^2 \left(2\tilde{g}_{\alpha\alpha}|\varphi_0^\alpha|^2 + \tilde{g}_{\alpha\beta}|\varphi_0^\beta|^2 \right) \\ & \qquad \times \int_0^t ds \left(\tilde{g}_{\alpha\alpha}|\varphi_0^\alpha(s)|^2 + \tilde{g}_{\alpha\beta}|\varphi_0^\beta(s)|^2 \right) G_T(t-s)\varphi_0^\alpha(s) \\ & + \epsilon^2 \eta_T^2 \tilde{g}_{\alpha\alpha}(\varphi_0^\alpha)^2 \int_0^t ds \left(\tilde{g}_{\alpha\alpha}|\varphi_0^\alpha(s)|^2 + \tilde{g}_{\alpha\beta}|\varphi_0^\beta(s)|^2 \right) G_T^*(t-s)\varphi_0^{\alpha *}(s) \\ & + \epsilon^2 \eta_T^2 \tilde{g}_{\alpha\beta}\varphi_0^\alpha \int_0^t ds \left(\tilde{g}_{\beta\beta}|\varphi_0^\beta(s)|^2 + \tilde{g}_{\beta\alpha}|\varphi_0^\alpha(s)|^2 \right) \Big(\varphi_0^\beta G_T^*(t-s)\varphi_0^{\beta *}(s) \\ & \qquad + \varphi_0^{\beta *} G_T(t-s)\varphi_0^\beta(s) \Big) \\ & + \epsilon^2 I_0^\alpha(t). \end{aligned} \tag{11}$$

Here

$$G_T(t) = -\frac{i}{\hbar} \sum_{n=1}^{\infty} \frac{\langle \xi_0^3|\xi_n\rangle^2}{\eta_T^2} e^{-i(E_n-E_0)t/\hbar} \tag{12}$$

is a temporal response function that comes from changes in the transverse wave function and that oscillates at the bare transverse eigenfrequencies, and

$$\begin{aligned} I_0^\alpha(t) = {}& \left(2\tilde{g}_{\alpha\alpha}|\varphi_0^\alpha|^2 + \tilde{g}_{\alpha\beta}|\varphi_0^\beta|^2\right) \sum_{n=1}^{\infty} \langle \xi_0^3|\xi_n\rangle \varphi_n^\alpha(0) e^{-i(E_n-E_0)t/\hbar} \\ & + \tilde{g}_{\alpha\alpha}(\varphi_0^\alpha)^2 \sum_{n=1}^{\infty} \langle \xi_0^3|\xi_n\rangle \varphi_n^{\alpha *}(0) e^{i(E_n-E_0)t/\hbar} \\ & + \tilde{g}_{\alpha\beta}\varphi_0^\alpha \sum_{n=1}^{\infty} \langle \xi_0^3|\xi_n\rangle \left(\varphi_0^\beta \varphi_n^{\beta *}(0) e^{i(E_n-E_0)t/\hbar} + \varphi_0^{\beta *}\varphi_n^\beta(0) e^{-i(E_n-E_0)t/\hbar}\right) \end{aligned} \tag{13}$$

is the term associated with the initial condensate wave function.

Equations (10) and (11) are the final result of the relative-state method. Not surprisingly, φ_0^α satisfies to lowest order the idealized reduced-dimension description of the time-dependent GP equations discussed in Sec. 2. The higher-order terms, on the other hand, introduce corrections to the reduced-dimension approximation that act as effective three-body, attractive, intra- and inter-mode interactions. These interactions are mediated by the changes in the transverse wave function and take place on the transverse time scales contained in the temporal response function G_T.

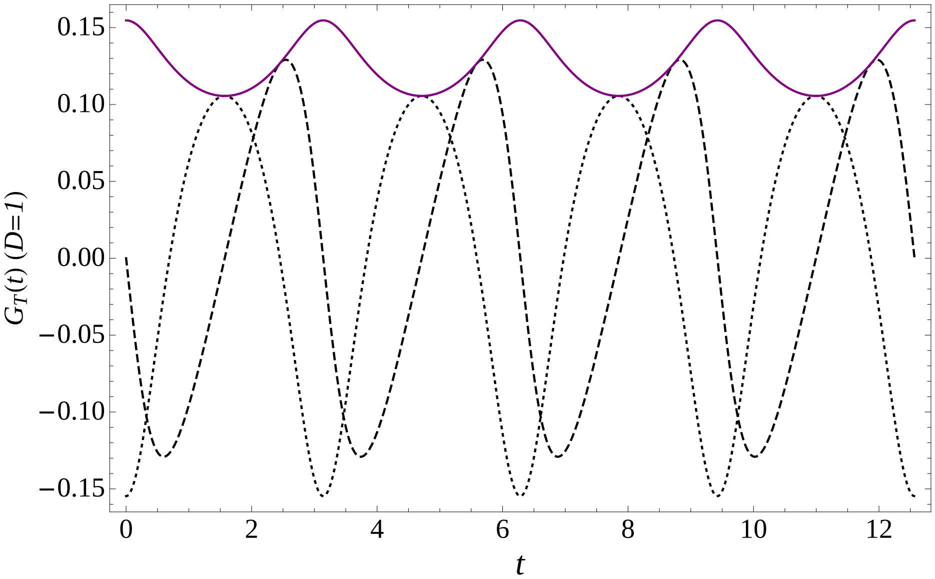

Figure 1. Temporal response function G_T, in units of $\hbar^{-1}$, for a pancake-like trap ($D = 1$) and a transverse harmonic potential. Time is measured in units of ω_T^{-1}. The dashed, black line represents the real part of G_T, the dotted, black line is the imaginary part, and the solid, purple line is the absolute value of G_T. G_T is a periodic function with fundamental oscillation frequency equal to $2\omega_T$. The anharmonicity of G_T essentially comes from the lowest two nonvanishing modes in the spectral decomposition (12), as shown in Fig. 3.

Interestingly, the temporal response function (12) has a closed-form solution for the case of a transverse harmonic potential. In this case, the transverse ground-state wave

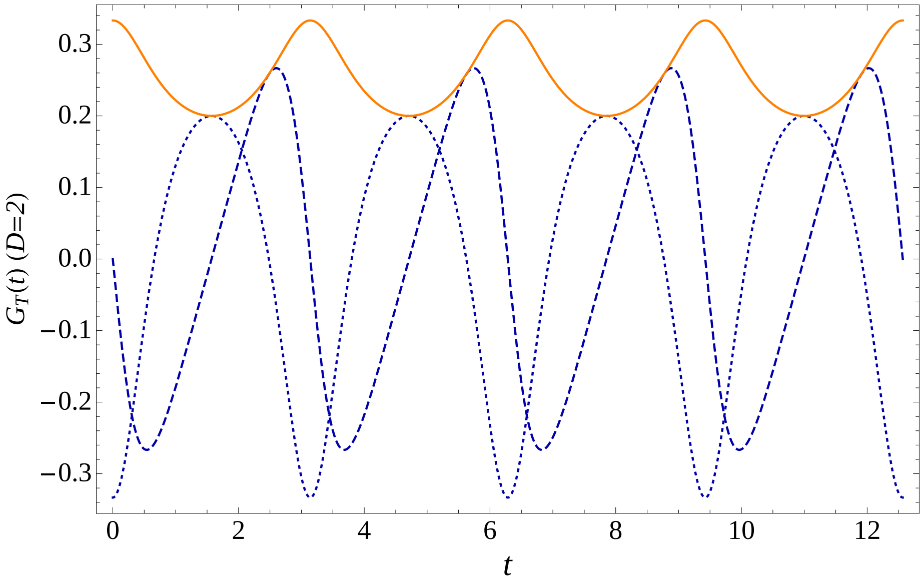

Figure 2. Temporal response function G_T, in units of $\hbar^{-1}$, for a cigar-shaped trap ($D = 2$) and a transverse harmonic potential. Time is measured in units of ω_T^{-1}. The dashed, blue line represents the real part of G_T, the dotted, blue line corresponds to the imaginary part, and the solid, orange line is the absolute value of G_T. As in the $D = 1$ case, the temporal response function G_T for a cigar-shaped BEC is a periodic function with fundamental oscillation frequency equal to $2\omega_T$. The anharmonicity of G_T is mainly due to the lowest two nonvanishing modes in the spectral decomposition (12) (see Fig. 3).

function is the Gaussian

$$\xi_0(\boldsymbol{\rho}) = \frac{e^{-\rho^2/2\rho_0^2}}{(\pi\rho_0^2)^{D/4}}, \tag{14}$$

where $\rho_0 = \sqrt{\hbar/m\omega_T}$, with ω_T being the transverse trap frequency. It is easy to see that

$$\eta_T = \left(\frac{1}{\sqrt{2\pi}\rho_0}\right)^D. \tag{15}$$

Moreover, for a pancake-like potential ($D = 1$), we have

$$\langle\xi_n|\xi_0^3\rangle = \begin{cases} \dfrac{(-1)^{n/2}}{\sqrt{\pi\, n!}}\eta_T\Gamma\left(\dfrac{n+1}{2}\right), & n \text{ even}, \\ 0, & n \text{ odd}. \end{cases} \tag{16}$$

For a cigar ($D = 2$), if we use polar coördinates for the transverse eigenfunctions, they take the form $\xi_{n_r m}(\rho, \varphi)$, with n_r and m being radial and azimuthal quantum numbers and with the eigenenergies given by $E_{n_r m} = \hbar\omega_T(2n_r + |m| + 1)$. Then we find that

$$\langle\xi_{n_r m}|\xi_{00}^3\rangle = 2^{-n_r}\eta_T\delta_{m0}. \tag{17}$$

By using Eqs. (16) and (17), we can write the response function as

$$G_T(t) = \begin{cases} \dfrac{i}{\hbar}\left(1 - \dfrac{2}{\sqrt{4 - e^{-2i\omega_T t}}}\right), & D = 1 \text{ (pancake)}, \\ \dfrac{i}{\hbar}\dfrac{1}{1 - 4e^{2i\omega_T t}}, & D = 2 \text{ (cigar)}. \end{cases} \tag{18}$$

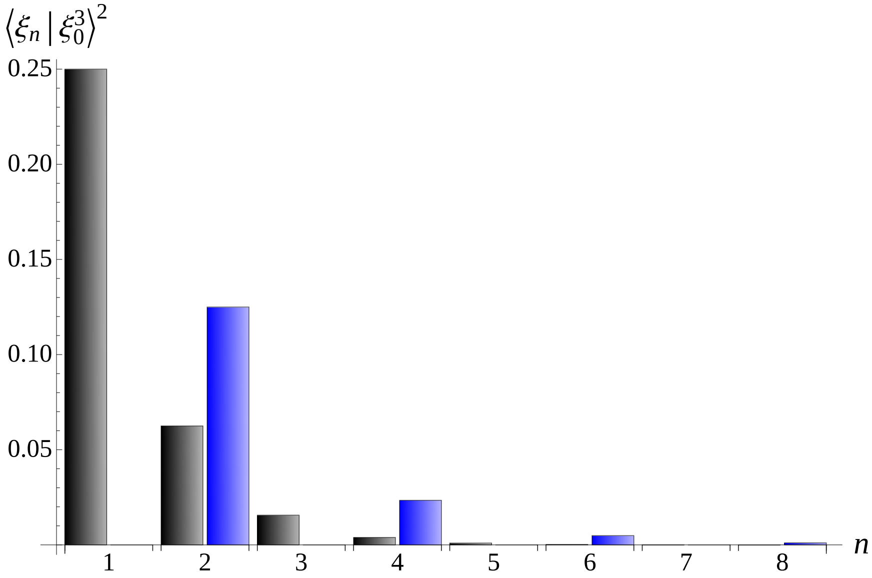

Figure 3. Value of the coefficients $\langle \xi_0^3 | \xi_n \rangle^2$ (in units of η_T^2) for a harmonic transverse trap for the first eight terms in the series (12). For every n, we show the value of the coefficient for a cigar-shaped potential (black bar on the left) as well as for a pancake-like trap (blue bar on the right). For a quasi-1D potential ($D = 2$), n represents the radial quantum number of the harmonic potential. For both cases, the spectral representation of G_T reveals a single dominant mode, namely $n = 1$ for a cigar and $n = 2$ for a pancake-like potential, that oscillates with frequency equal to $2\omega_T$. The remaining, smaller terms introduce the small anharmonicity seen in Figs. 1 and 2.

Figures 1 and 2 show the temporal response function (18) for 2D and 1D trap geometries. For both trap geometries, the fundamental oscillation frequency of G_T is equal to $2\omega_T$. The anharmonicity of G_T is better understood from the spectral representation (12). Figure 3 shows the value of the coefficients $\langle \xi_0^3 | \xi_n \rangle^2$ for the first few terms in the series expansion (12); this reveals the dominant mode, with frequency equal to $2\omega_T$, and the remaining smaller terms responsible for the anharmonicity in Figs. 1 and 2. Note that in the case of a pancake-like potential ($D = 1$), the well-defined parity of the transverse ground state requires ξ_0^3 to be orthogonal to states with odd parity. Therefore, the dominant mode in the decomposition (12) corresponds to the $n = 2$ term.

4. Adiabatic elimination of φ_n^α

Due to the high anisotropy of the trapping potential, we expect the evolution of the longitudinal modes to take place on a much longer time scale than the transverse modes. In fact, our perturbation expansion is valid as long as this assumption holds, for according to Eq. (11), $\dot{\varphi}_0^\alpha = O(\epsilon)$. In this section, we use this result to derive an adiabatic approximation for φ_n^α, which we then use to bring Eq. (11) to a more tractable form.

We start by integrating Eq. (10) by parts, which lets us write the following relation for $\varphi_n^\alpha(t)$, $n \geq 1$:

$$\begin{aligned} &\varphi_n^\alpha(t) - \varphi_n^\alpha(0) e^{-i(E_n - E_0)t/\hbar} \\ &\qquad = -\frac{\langle \xi_n | \xi_0^3 \rangle}{E_n - E_0} e^{-i(E_n - E_0)(t-s)/\hbar} \left(\tilde{g}_{\alpha\alpha} |\varphi_0^\alpha(s)|^2 + \tilde{g}_{\alpha\beta} |\varphi_0^\beta(s)|^2 \right) \varphi_0^\alpha(s) \Big|_0^t + O(\epsilon). \quad (19) \end{aligned}$$

Here the first term on the right-hand side arises from the straightforward integration of the rapidly oscillating exponential in Eq. (10), whereas the (neglected) remaining term is of higher order in ϵ because it involves time derivatives of φ_0^α and $\varphi_0^{\alpha *}$. We assume from now on, consistent with our perturbation theory, that these higher-order terms in Eq. (19) can be neglected. Under this approximation, we write

$$\varphi_n^\alpha(t) \simeq \tilde{\varphi}_n^\alpha(t) + \tilde{I}_n^\alpha(t), \tag{20}$$

where

$$\tilde{\varphi}_n^\alpha(t) = -\frac{\langle \xi_n | \xi_0^3 \rangle}{E_n - E_0} \left(\tilde{g}_{\alpha\alpha} |\varphi_0^\alpha(t)|^2 + \tilde{g}_{\alpha\beta} |\varphi_0^\beta(t)|^2 \right) \varphi_0^\alpha(t) \tag{21}$$

corresponds to the adiabatic following of $|\varphi_0^\alpha|^2 \varphi_0^\alpha$ and $|\varphi_0^\beta|^2 \varphi_0^\alpha$, which is the dominant dynamical effect described by Eq. (19). The remaining lowest-order term,

$$\tilde{I}_n^\alpha(t) = \left(\varphi_n^\alpha(0) - \tilde{\varphi}_n^\alpha(0) \right) e^{-i(E_n - E_0)t/\hbar}, \tag{22}$$

is associated with the deviation of $\varphi_n^\alpha(0)$, the projection of the initial condensate wave function onto ξ_n, from its adiabatic variant $\tilde{\varphi}_n^\alpha(0)$.

We can now use the adiabatic approximation (20) to eliminate $\varphi_n^\alpha(t)$, $n \geq 1$, from Eq. (8), thus obtaining a more tractable evolution equation for φ_0^α than Eq. (11):

$$\begin{aligned} i\hbar \dot{\varphi}_0^\alpha = {} & \epsilon \left(H_L + \tilde{g}_{\alpha\alpha} \eta_T |\varphi_0^\alpha|^2 + \tilde{g}_{\alpha\beta} \eta_T |\varphi_0^\beta|^2 \right) \varphi_0^\alpha \\ & - \epsilon^2 \Upsilon_T \left(3\tilde{g}_{\alpha\alpha} |\varphi_0^\alpha|^2 + \tilde{g}_{\alpha\beta} |\varphi_0^\beta|^2 \right) \left(\tilde{g}_{\alpha\alpha} |\varphi_0^\alpha|^2 + \tilde{g}_{\alpha\beta} |\varphi_0^\beta|^2 \right) \varphi_0^\alpha \\ & - 2\epsilon^2 \Upsilon_T \tilde{g}_{\alpha\beta} \varphi_0^\alpha |\varphi_0^\beta|^2 \left(\tilde{g}_{\beta\beta} |\varphi_0^\beta|^2 + \tilde{g}_{\beta\alpha} |\varphi_0^\alpha|^2 \right) + \epsilon^2 \tilde{I}_0^\alpha, \end{aligned} \tag{23}$$

where

$$\begin{aligned} \tilde{I}_0^\alpha = {} & \sum_{n=1}^{\infty} \langle \xi_0^3 | \xi_n \rangle \\ & \times \Big[\left(2\tilde{g}_{\alpha\alpha} |\varphi_0^\alpha|^2 + \tilde{g}_{\alpha\beta} |\varphi_0^\beta|^2 \right) \tilde{I}_n^\alpha + \tilde{g}_{\alpha\alpha} (\varphi_0^\alpha)^2 \tilde{I}_n^{\alpha *} + \tilde{g}_{\alpha\beta} \varphi_0^\alpha \left(\varphi_0^\beta \tilde{I}_n^{\beta *} + \varphi_0^{\beta *} \tilde{I}_n^\beta \right) \Big]. \end{aligned} \tag{24}$$

The coupling parameter Υ_T in Eq. (23), defined by

$$\Upsilon_T \equiv \sum_{n=1}^{\infty} \frac{\langle \xi_n | \xi_0^3 \rangle^2}{E_n - E_0} \geq 0, \tag{25}$$

is determined solely by the properties of the transverse trap and characterizes the strength of the coupling of transverse and longitudinal directions. The quantity η_T^2/Υ_T can be thought of as the relevant quantification of the transverse energy scale as far as the perturbation theory is concerned.

After reorganizing the second-order terms in Eq. (23), we obtain the final form of the effective, coupled, two-mode evolution equation for the dominant longitudinal wave function φ_0^α,

$$\begin{aligned} i\hbar\dot{\varphi}_0^\alpha = {} & \epsilon \left(H_L + \tilde{g}_{\alpha\alpha}\eta_T|\varphi_0^\alpha|^2 + \tilde{g}_{\alpha\beta}\eta_T|\varphi_0^\beta|^2 \right) \varphi_0^\alpha \\ & - \epsilon^2 \Upsilon_T \Big(3\tilde{g}_{\alpha\alpha}^2 |\varphi_0^\alpha|^4 + (4\tilde{g}_{\alpha\alpha} + 2\tilde{g}_{\beta\alpha})\tilde{g}_{\alpha\beta}|\varphi_0^\alpha|^2|\varphi_0^\beta|^2(\tilde{g}_{\alpha\beta} + 2\tilde{g}_{\beta\beta})|\varphi_0^\beta|^4 \Big) \varphi_0^\alpha \\ & + \epsilon^2 \tilde{I}_0^\alpha, \end{aligned} \tag{26}$$

where

$$\begin{aligned} \tilde{I}_0^\alpha = {} & \left(2\tilde{g}_{\alpha\alpha}|\varphi_0^\alpha|^2 + \tilde{g}_{\alpha\beta}|\varphi_0^\beta|^2 \right) (\Phi^\alpha - \tilde{\Phi}^{\alpha\beta}) + \tilde{g}_{\alpha\alpha}(\varphi_0^\alpha)^2(\Phi^{\alpha*} - \tilde{\Phi}^{\alpha\beta*}) \\ & + \tilde{g}_{\alpha\beta}\varphi_0^\alpha \left[\varphi_0^\beta(\Phi^{\beta*} - \tilde{\Phi}^{\beta\alpha*}) + \varphi_0^{\beta*}(\Phi^\beta - \tilde{\Phi}^{\beta\alpha}) \right]. \end{aligned} \tag{27}$$

Here we introduce the functions

$$\Phi^\alpha(t) = \sum_{n=1}^{\infty} \langle \xi_n | \xi_0^3 \rangle \varphi_n^\alpha(0) e^{-i(E_n - E_0)t/\hbar}, \tag{28}$$

$$\tilde{\Phi}^{\alpha\beta}(t) = -\left(\tilde{g}_{\alpha\alpha}|\varphi_0^\alpha(0)|^2 + \tilde{g}_{\alpha\beta}|\varphi_0^\beta(0)|^2 \right) \varphi_0^\alpha(0) \upsilon_T(t), \tag{29}$$

$$\upsilon_T(t) = \sum_{n=1}^{\infty} \frac{\langle \xi_n | \xi_0^3 \rangle^2}{E_n - E_0} e^{-i(E_n - E_0)t/\hbar}. \tag{30}$$

Notice that $\upsilon_T(0) = \Upsilon_T$ and $\dot{\upsilon}_T(t) = \eta_T^2 G_T(t)$.

The importance of the source term $\tilde{I}_0^\alpha$ in determining the dynamical behavior of φ_0^α essentially depends on the difference between $\varphi_n^\alpha(0)$ and $\tilde{\varphi}_n^\alpha(0)$. As shown by Eqs. (28) and (29), $\tilde{I}_0^\alpha$ is a rapidly varying function in comparison to the other terms in Eq. (26). In the case of a transverse harmonic confinement, we can write $\upsilon_T(t)$ in the closed form

$$\upsilon_T(t) = \begin{cases} -\dfrac{\eta_T^2}{\hbar\omega_T} \ln \left[\dfrac{1}{2} \left(1 + \sqrt{1 - \dfrac{1}{4} e^{-2i\omega_T t}} \right) \right], & D = 1 \text{ (pancake)}, \\ -\dfrac{\eta_T^2}{2\hbar\omega_T} \ln \left(1 - \dfrac{1}{4} e^{-2i\omega_T t} \right), & D = 2 \text{ (cigar)}. \end{cases} \tag{31}$$

The absolute value and real and imaginary parts of υ_T are plotted in Fig. 4 for $D = 1$ and Fig. 5 for $D = 2$.

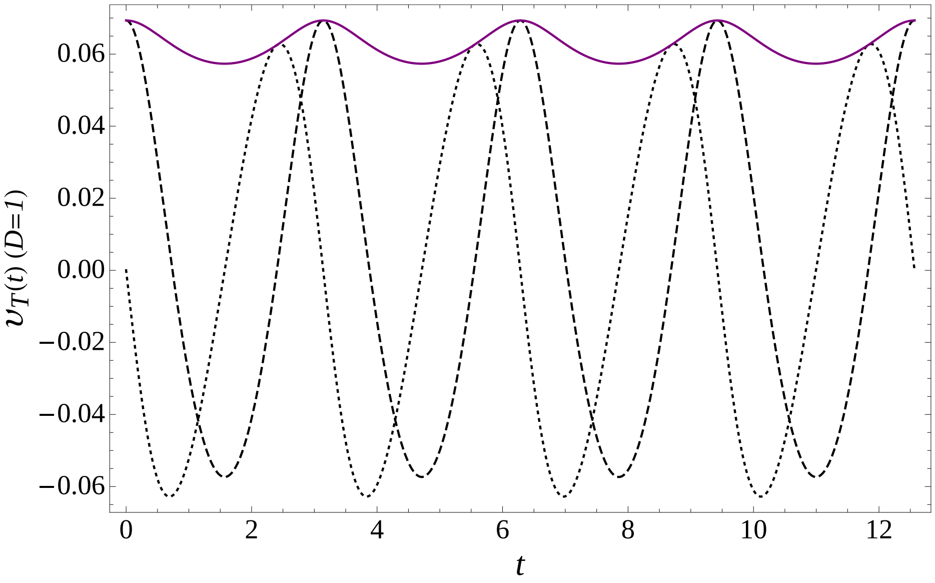

Figure 4. Plots of υ_T, in units of $(\hbar\omega_T/\eta_T^2)^{-1}$, as a function of time for a pancake-like geometry ($D = 1$) and transverse harmonic potential. Time is measured in units of ω_T^{-1}. The dashed, black line represents the real part of υ_T, the dotted, black line is the imaginary part, and the solid, purple line is the absolute value.

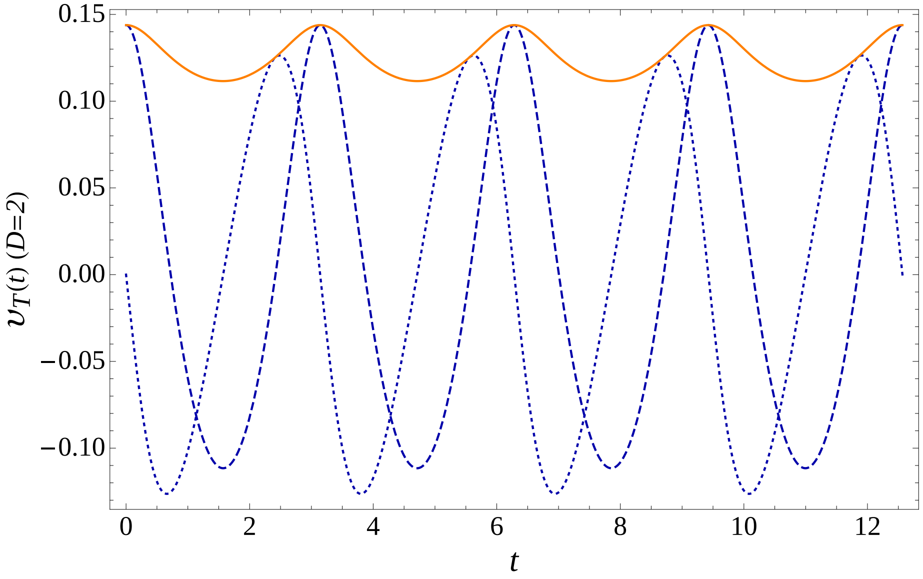

Figure 5. Plots of υ_T, in units of $(\hbar\omega_T/\eta_T^2)^{-1}$, as a function of time for a cigar-shaped trap ($D = 2$) with a transverse harmonic potential. Time is measured in units of ω_T^{-1}. The dashed, blue line represents the real part of υ_T, the dotted, blue line is the imaginary part, and the solid, orange line is the absolute value.

4.1. Single-mode dynamics within the adiabatic elimination of φ_n^α

The dynamical equations for a single-mode BEC can be obtained trivially from Eqs. (20) and (26). By simply setting $\tilde{g}_{\alpha\beta} = 0$ and dropping the superfluous index α, we get

$$\varphi_n = -\frac{\langle \xi_n | \xi_0^3 \rangle}{E_n - E_0} \tilde{g} |\varphi_0|^2 \varphi_0 + \tilde{I}_n = \tilde{\varphi}_n + \tilde{I}_n, \quad n \geq 1, \tag{32}$$

$$i\hbar\dot{\varphi}_0 = \epsilon \left(H_L + \tilde{g}\eta_T |\varphi_0|^2 - 3\epsilon \tilde{g}^2 \Upsilon_T |\varphi_0|^4 \right) \varphi_0 + \epsilon^2 \tilde{I}_0, \tag{33}$$

where

$$\tilde{I}_n = \big(\varphi_n(0) - \tilde{\varphi}_n(0) \big) e^{-i(E_n - E_0)t/\hbar}, \tag{34}$$

$$\tilde{I}_0 = 2\tilde{g} |\varphi_0|^2 (\Phi - \tilde{\Phi}) + \tilde{g} \varphi_0^2 (\Phi^* - \tilde{\Phi}^*), \tag{35}$$

and

$$\Phi(t) = \sum_{n=1}^{\infty} \langle \xi_n | \xi_0^3 \rangle \varphi_n(0) e^{-i(E_n - E_0)t/\hbar}, \tag{36}$$

$$\tilde{\Phi}(t) = -\tilde{g} |\varphi_0(0)|^2 \varphi_0(0) \upsilon_T(t). \tag{37}$$

Equations (32) and (33) correspond to the time-dependent versions of the stationary single-mode case [8], but with the additional source terms $\tilde{I}_n$ and $\tilde{I}_0$. In fact, in the stationary case, $\varphi_n = \tilde{\varphi}_n$, and hence $\Phi = \tilde{\Phi}$. As a result, both $\tilde{I}_n$ and $\tilde{I}_0$ vanish and the questions reduce to that of Ref. [8]. Note that relative to a GP equation, the longitudinal equation (33) has an additional quintic term, which acts as an effective three-body, attractive interaction among the atoms regardless of the sign of g. This attractive interaction is mediated by the changes in the transverse wave function, as evidenced by the appearance of the (nonnegative) coupling parameter Υ_T in the coupling strength $3g^2\Upsilon_T$.

The coupling constants in Eq. (33) can be calculated explicitly for a transverse harmonic potential. It follows from Eqs. (16), (17), and (25) that

$$\Upsilon_T = \begin{cases} \dfrac{\eta_T^2}{\hbar\omega_T} \ln(8 - 4\sqrt{3}), & D = 1 \text{ (pancake)}, \\[2ex] \dfrac{\eta_T^2}{2\hbar\omega_T} \ln\dfrac{4}{3}, & D = 2 \text{ (cigar)}. \end{cases} \tag{38}$$

As a result, the coupling constants for a cigar-shaped trap ($d = 1$) are $g\eta_T = 2\hbar\omega_T a$ and $3g^2\Upsilon_T = 6\hbar\omega_T a^2 \ln(4/3)$, whereas for a quasi-2D pancake ($d = 2$), we obtain $g\eta_T = 2\sqrt{2\pi}\hbar\omega_T \rho_0 a$ and $3g^2\Upsilon_T = 24\pi\hbar\omega_T \rho_0^2 a^2 \ln(8 - 4\sqrt{3})$.

It is worth pointing out that such a self-focusing interaction has also been used to study the propagation of solitons in single-mode, attractive, quasi-1D condensates, trapped by an infinitely long cylindrical harmonic potential [9, 10, 11]. In contrast to using a relative-state decomposition of the three-dimensional condensate wave function, those studies use a Taylor expansion of a local, transverse chemical potential about the maximum density of the condensate to derive the additional quintic nonlinearity. This leads to an equation without the source term $\tilde{I}_0$ and with a coupling constant that differs from $3g^2\Upsilon_T$ (for $d=1$) by a factor of 4. This factor corresponds to the difference between using the maximum of the Gaussian ground-state probability distribution and the average η_T of the distribution over itself.

5. Two-mode dynamics of a cigar-shaped ^{87}Rb condensate

In this section we apply the general results of the time-dependent relative-state decomposition derived above to analyze the two-mode dynamics of a cigar-shaped ^{87}Rb condensate consisting of N atoms that can occupy the $5S_{1/2}$ $|F=1;\, M_F=-1\rangle$ and $|F=2;\, M_F=+1\rangle$ hyperfine states. These states are of particular interest to us because they can be used to implement a nonlinear Ramsey interferometry protocol with sensitivity that scales better than $1/N$, as discussed previously in Refs. [2, 4, 5, 6].

5.1. Two-mode evolution

In typical experiments [12, 13, 14, 15, 16, 17, 18], the $|F=1;\, M_F=-1\rangle \equiv |1\rangle$ state is trapped and cooled to the condensation point. Once the atoms in $|1\rangle$ have accumulated in the condensate ground state, a two-photon drive is used to couple the $|1\rangle$ state to the $|F=2;\, M_F=+1\rangle \equiv |2\rangle$ state. These two states have nearly identical magnetic moments, and hence feel essentially the same confining potentials. This strategy is used instead of cooling the two hyperfine states simultaneously to form a condensate in a superposition, because the lifetime of atoms in the $|2\rangle$ state in a trap is much shorter than the lifetime of atoms in the $|1\rangle$ state. Thus, we assume from now on that the optical pulse suddenly creates the superposition state $\psi(\mathbf{r})(|1\rangle+|2\rangle)/\sqrt{2}$ for each atom.‡ This procedure creates the two-mode condensate with both modes being occupied by the same number of atoms and having the same initial wave function $\psi(\mathbf{r})$. In this case, the inter-mode coupling is symmetric, i.e., $\tilde{g}_{12}=\tilde{g}_{21}=g_{12}(N-1)/2$, and we can write the longitudinal two-mode equations (26) as

$$
\begin{aligned}
i\hbar\dot{\varphi}_0^1 = \epsilon & \left(H_L + \tilde{g}_{11}\eta_T|\varphi_0^1|^2 + \tilde{g}_{12}\eta_T|\varphi_0^2|^2\right)\varphi_0^1 \\
& - \epsilon^2\Upsilon_T\Big(3\tilde{g}_{11}^2|\varphi_0^1|^4 + (4\tilde{g}_{11}+2\tilde{g}_{12})\tilde{g}_{12}|\varphi_0^1|^2|\varphi_0^2|^2 + \tilde{g}_{12}(\tilde{g}_{12}+2\tilde{g}_{22})|\varphi_0^2|^4\Big)\varphi_0^1 \\
& + \epsilon^2\tilde{I}_0^1,
\end{aligned}
\qquad (39)
$$

---

‡ This approximation holds as long as the Rabi-flopping time scale for the atomic transition is smaller than the time scale for the transverse BEC dynamics (the longitudinal BEC dynamics occurs on an even longer time scale). For the ^{87}Rb BECs we consider here, the Rabi-flopping time scale is typically less than a millisecond, so these conditions hold for the trapping potentials we consider here.

$$\begin{aligned} i\hbar\dot{\varphi}_0^2 &= \epsilon\left(H_L + \tilde{g}_{22}\eta_T|\varphi_0^2|^2 + \tilde{g}_{12}\eta_T|\varphi_0^1|^2\right)\varphi_0^2 \\ &\quad - \epsilon^2\Upsilon_T\Big(3\tilde{g}_{22}^2|\varphi_0^2|^4 + (4\tilde{g}_{22} + 2\tilde{g}_{12})\tilde{g}_{12}|\varphi_0^2|^2|\varphi_0^1|^2 + \tilde{g}_{12}(\tilde{g}_{12} + 2\tilde{g}_{11})|\varphi_0^1|^4\Big)\varphi_0^2 \\ &\quad + \epsilon^2\tilde{I}_0^2, \end{aligned} \tag{40}$$

which, of course, are written under the assumption that the longitudinal functions $\varphi_n^1(t)$ and $\varphi_n^2(t)$ can be approximated by Eq. (20) and, hence, are given by

$$\varphi_n^1(t) = -\frac{\langle\xi_n|\xi_0^3\rangle}{E_n - E_0}\left(\tilde{g}_{11}|\varphi_0^1(t)|^2 + \tilde{g}_{12}|\varphi_0^2(t)|^2\right)\varphi_0^1(t) + \tilde{I}_n^1(t), \tag{41}$$

$$\varphi_n^2(t) = -\frac{\langle\xi_n|\xi_0^3\rangle}{E_n - E_0}\left(\tilde{g}_{22}|\varphi_0^2(t)|^2 + \tilde{g}_{12}|\varphi_0^1(t)|^2\right)\varphi_0^2(t) + \tilde{I}_n^2(t). \tag{42}$$

Before we write down the expressions for the source terms in the equations above, we use below the results from the relative-state decomposition of the ground-state wave function, derived in [8], to bring $\tilde{I}_0^1$, $\tilde{I}_0^2$, $\tilde{I}_n^1$, and $\tilde{I}_n^2$ to a simpler form.

In our mean-field model, we suppose that all N atoms initially occupy the same single-particle wave function $\psi(\boldsymbol{\rho}, \boldsymbol{r})$, which is the solution of the time-independent, three-dimensional GP equation for the state $|1\rangle$. For this particular choice of the initial state, we showed in [8] that, in the perturbative regime $N \ll \mathcal{N}_T$, the condensate wave function can be approximated, to first order in perturbation theory, by the time-independent relative-state decomposition

$$\psi(\boldsymbol{\rho}, \boldsymbol{r}) = \xi_0(\boldsymbol{\rho})\varphi_0(\boldsymbol{r}) + \epsilon\sum_{n=1}^{\infty}\xi_n(\boldsymbol{\rho})\varphi_n(\boldsymbol{r}) = \psi^1(t=0) = \psi^2(t=0), \tag{43}$$

where the dominant longitudinal wave function $\varphi_0(\boldsymbol{r})$ is the solution to

$$(\tilde{\mu}_L - H_L - \tilde{g}\eta_T\varphi_0^2 + 3\epsilon\tilde{g}^2\Upsilon_T\varphi_0^4)\varphi_0 = 0, \tag{44}$$

with $\tilde{g} = (N-1)g_{11}$, and

$$\varphi_{n0} = -\tilde{g}\varphi_{00}^3\frac{\langle\xi_0^3|\xi_n\rangle}{E_n - E_0} = \varphi_n^1(t=0) = \varphi_n^2(t=0). \tag{45}$$

Here φ_{00} is the zero-order longitudinal wave function given by the reduced-dimension, single-mode GP equation

$$(\mu_L - H_L - \tilde{g}\eta_T\varphi_{00}^2)\varphi_{00} = 0. \tag{46}$$

Thus, using Eq. (45), we can write Eq. (20) as

$$\tilde{I}_n^\alpha(t) = -\big(\tilde{g} - \tilde{g}_{\alpha\alpha} - \tilde{g}_{\alpha\beta}\big)\varphi_{00}^3\frac{\langle\xi_0^3|\xi_n\rangle}{E_n - E_0}e^{-i(E_n - E_0)t/\hbar} \tag{47}$$

and the functions (28) and (29) as

$$\Phi^1(t) = \Phi^2(t) = -\tilde{g}\varphi_{00}^3\boldsymbol{\upsilon}_T(t), \tag{48}$$

$$\tilde{\Phi}^{\alpha\beta}(t) = -\left(\tilde{g}_{\alpha\alpha} + \tilde{g}_{\alpha\beta}\right)\varphi_{00}^3\boldsymbol{\upsilon}_T(t). \tag{49}$$

In Eq. (49), we used that $\upvarphi_0^\alpha(0) = \varphi_{00} + O(\epsilon)$ and kept only the lowest-order terms, considering that the source terms are of quadratic order in ϵ. From Eqs. (48) and (49), it follows trivially that

$$\Phi^1 - \tilde{\Phi}^{12} = -(\tilde{g} - \tilde{g}_{11} - \tilde{g}_{12})\varphi_{00}^3 \upsilon_T(t), \tag{50}$$

$$\Phi^2 - \tilde{\Phi}^{21} = -(\tilde{g} - \tilde{g}_{22} - \tilde{g}_{12})\varphi_{00}^3 \upsilon_T(t). \tag{51}$$

For our particular choice of the hyperfine levels of ^{87}Rb, the s-wave scattering lengths for the processes $|1\rangle|1\rangle \rightarrow |1\rangle|1\rangle$, $|1\rangle|2\rangle \rightarrow |1\rangle|2\rangle$, and $|2\rangle|2\rangle \rightarrow |2\rangle|2\rangle$, respectively, are $a_{11} = 100.40a_0$, $a_{12} = 97.66a_0$, and $a_{22} = 95.00a_0$ [15], with a_0 being the Bohr radius. Thus, the inter-mode coupling is given approximately by the arithmetic mean of the intra-mode coefficients, i.e., $g_{12} \approx (g_{11} + g_{22})/2$, which equivalently means that

$$g_{11} - g_{12} \approx (g_{11} - g_{22})/2 \equiv \gamma_1. \tag{52}$$

Therefore, it follows that

$$\tilde{g} - \tilde{g}_{11} - \tilde{g}_{12} = \frac{1}{2}(g_{11} - g_{12})(N-1) \approx 2\gamma_1(N-1), \tag{53}$$

$$\tilde{g} - \tilde{g}_{22} - \tilde{g}_{12} = \frac{1}{2}(2g_{11} - g_{12} - g_{22})(N-1) \approx 3\gamma_1(N-1). \tag{54}$$

We can now put all these results together with Eqs. (27) and (47) to write all the source terms as

$$\begin{aligned}\tilde{I}_0^1(t) = -2\gamma_1(N-1)\varphi_{00}^3 \Big\{ &\left(2\tilde{g}_{11}|\upvarphi_0^1(t)|^2 + \tilde{g}_{12}|\upvarphi_0^2(t)|^2\right)\upsilon_T(t) + \tilde{g}_{11}(\upvarphi_0^1(t))^2\upsilon_T^*(t) \\ &+ \frac{3}{2}\tilde{g}_{12}\upvarphi_0^1(t)\left[\upvarphi_0^2(t)\upsilon_T^*(t) + \upvarphi_0^{2*}(t)\upsilon_T(t)\right]\Big\},\end{aligned} \tag{55}$$

$$\begin{aligned}\tilde{I}_0^2(t) = -3\gamma_1(N-1)\varphi_{00}^3 \Big\{ &\left(2\tilde{g}_{22}|\upvarphi_0^2(t)|^2 + \tilde{g}_{12}|\upvarphi_0^1(t)|^2\right)\upsilon_T(t) + \tilde{g}_{22}(\upvarphi_0^2(t))^2\upsilon_T^*(t) \\ &+ \frac{1}{3}\tilde{g}_{12}\upvarphi_0^2(t)\left[\upvarphi_0^1(t)\upsilon_T^*(t) + \upvarphi_0^{1*}(t)\upsilon_T(t)\right]\Big\},\end{aligned} \tag{56}$$

$$\tilde{I}_n^1(t) = -2\gamma_1(N-1)\varphi_{00}^3 \frac{\langle \xi_0^3|\xi_n\rangle}{E_n - E_0} e^{-i(E_n - E_0)t/\hbar}, \tag{57}$$

$$\tilde{I}_n^2(t) = -3\gamma_1(N-1)\varphi_{00}^3 \frac{\langle \xi_0^3|\xi_n\rangle}{E_n - E_0} e^{-i(E_n - E_0)t/\hbar}. \tag{58}$$

Because $\gamma_1 \ll g_{22}, g_{12}, g_{11}$, however, we expect the contribution from all the source terms to the two-mode evolution to be negligible. In other words, since the initial longitudinal function $\varphi_n(0)$ is not much different from $\tilde{\upvarphi}_n^\alpha$, the evolution of $\upvarphi_n^\alpha$ should not differ much from the adiabatically tracking solutions.

5.2. Numerical simulations

To study the two-mode evolution described by our perturbative model, we numerically integrate Eqs. (39) and (40) and compare it against the exact numerical results for the evolution of the two-mode BEC, given by the two-mode, coupled, three-dimensional

Gross-Pitaevskii equations (1) [19]. We restrict our numerical analysis to the same scenario of the three-dimensional simulations presented in Ref. [5]. That is, we consider the two-mode condensate to be trapped by cigar-shaped potentials of the form

$$V(\rho, z) = \frac{1}{2}(m\omega_T^2\rho^2 + kz^q), \tag{59}$$

with $q = 2$, 4, and 10. These three potentials allow us to explore how the results vary due to the inhomogeneity of the trapping potentials. Notice that the limit $q \to \infty$ recovers the case of a homogeneous, hard-walled trap.

We set the transverse frequency to 350 Hz and the longitudinal frequency to 3.5 Hz for the harmonic case ($q = 2$), with the result that $\mathcal{N}_T \simeq 14\,000$ atoms. We obtain this estimate of $\mathcal{N}_T$ from the definition given in [5]. To compare the simulations for the different power-law potentials, we choose the stiffness parameter k so that $\mathcal{N}_T$ remains the same for the two other values of q; thus all the traps have the same one-dimensional regime of atom numbers. For such choice of parameters, we find $\rho_0 \simeq 0.6\,\mu$m and the aspect ratio of the bare traps (ρ_0:z_0) to be approximately equal to 1:10, 1:24, and 1:57, respectively, for $q = 2, 4, 10$.

5.3. Differential phase dynamics: nonlinear Ramsey interferometry

We are now in position to revisit the numerical simulations of a nonlinear Ramsey interferometer presented in Ref. [5] and use the results of the time-dependent relative-state decomposition to analyze the relative-phase dynamics of the two-mode condensate.

As in typical Ramsey interferometry schemes, the protocol runs as follows. The atoms are first condensed to the state $\psi(\mathbf{r})|1\rangle$, and a fast optical pulse suddenly creates the superposition state $\psi(\mathbf{r})(|1\rangle + |2\rangle)/\sqrt{2}$ for each atom. The atoms are then allowed to evolve freely for a time t, which brings the atomic state to $[\psi^1(\mathbf{r}, t)|1\rangle + \psi^2(\mathbf{r}, t)|2\rangle]/\sqrt{2}$. A second transition between the hyperfine levels is then used to transform any differential phases between the two modes into population information that is finally detected. For this second transition, we choose a $\pi/2$ rotation about the Bloch x axis, changing the atomic state to

$$\frac{1}{2}\big(\psi^1 - i\psi^2\big)|1\rangle - \frac{i}{2}\big(\psi^1 + i\psi^2\big)|2\rangle. \tag{60}$$

Thus any differential phases accumulated by the mean-field solutions will give rise to an interference fringe pattern in the detection probabilities for each hyperfine level,

$$p_{1,2} = \frac{1}{2}\big[1 \mp \mathrm{Im}(\langle\psi^2|\psi^1\rangle)\big], \tag{61}$$

due to the overlap of the two spatial wave functions,

$$\langle\psi^2|\psi^1\rangle = \int d^3r\, \psi^{2*}\psi^1. \tag{62}$$

Note that the imaginary part of the overlap (62) is responsible for the fringe pattern in this interferometry scheme.

5.4. Time scales

The relevant time scale for the relative-phase dynamics of the two-mode condensate can easily be estimated if one completely neglects the spatial evolution of the condensate. Under this approximation, the two-mode evolution becomes trivial. Due to the difference in scattering lengths, the only effect of the evolution is to introduce a differential phase shift between the states $|1\rangle$ and $|2\rangle$. This relative phase simply corresponds to the difference between the average scattering energies of the condensate, which implies that the detection probabilities (61) oscillate as

$$p_{1,2} = \frac{1}{2}\left[1 \mp \sin(\Omega_N t)\right], \tag{63}$$

where

$$\Omega_N = (N-1)\eta\gamma_1/\hbar \tag{64}$$

is the fringe frequency. Here the quantity

$$\eta = \int d^3r\, |\psi(\mathbf{r})|^4 \tag{65}$$

is a measure of the inverse volume occupied by the ground-state wave function. This fringe pattern allows one to estimate the coupling constant γ_1 with an uncertainty given by

$$\delta\gamma_1 = \frac{\langle(\Delta\hat{J}_y)^2\rangle^{1/2}}{|d\langle\hat{J}_y\rangle/d\gamma_1|} \sim \frac{1}{\sqrt{N}N\eta}, \tag{66}$$

whose scaling with the atom number is better than the optimal $1/N$ scaling of linear interferometry [5].

Within the reduced-dimension approximation of Eq. (3), the dominant contribution to the fringe frequency is

$$\Omega_{\mathrm{rda}} = N\eta_T\eta_L\gamma_1/\hbar, \tag{67}$$

where

$$\eta_L = \int d^d r\, |\varphi_{00}(\boldsymbol{r})|^4. \tag{68}$$

This frequency sets the characteristic time scale of the short-time relative evolution of the longitudinal wave functions φ_0^1 and φ_0^2.

In Fig. 6, we plot the values of the Ramsey fringe frequencies Ω_N and Ω_{rda}, as a function of the atom number and the three different values of q. We calculate Ω_N using the numerical evaluation of η. Not surprisingly, Ω_{rda} gives an upper bound on the numerical values of Ω_N. The important point here is not the difference between Ω_N and Ω_{rda}, but rather that both are much smaller than the transverse frequency ω_T, as is to be expected for the highly anisotropic potentials used in our simulations. This result indicates that the longitudinal frequencies do satisfy the adiabatic condition $\Omega_N, \Omega_{\mathrm{rda}} \ll \omega_T$. We therefore expect that the longitudinal two-mode equations (26) can be used to model the dynamics of the BEC interferometry protocol.

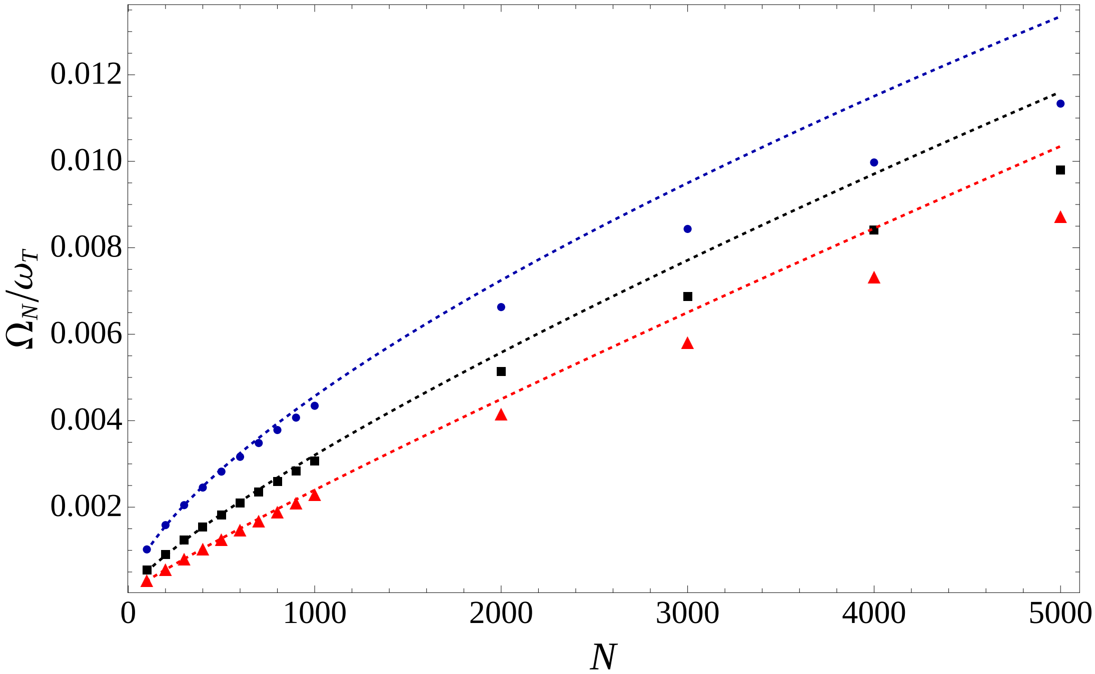

Figure 6. Idealized fringe frequency $\Omega_N = N\eta\gamma_1/\hbar$, in units of the bare transverse frequency ω_T, as a function of the number of condensed atoms. This fringe frequency, calculated using the numerical results for η, is plotted as circles (blue) for $q = 2$, squares (black) for $q = 4$, and triangles (red) for $q = 10$. The dashed lines correspond to the reduced-dimension estimate, $\Omega_{\rm rda} = N\eta_T\eta_L\gamma_1/\hbar$, which gives an upper-bound to the fringe frequency Ω_N calculated using the numerical results for η. Both frequencies are much smaller than the transverse trap frequency ω_T.

5.4.1. Ramsey fringes. According to the relative-state decomposition (6), it is easy to see that, at the order we are working, the dominant longitudinal functions φ_0^1 and φ_0^2 carry all the information about the relative phase between the three-dimensional condensate wave functions ψ^2 and ψ^1, since

$$\langle\psi^2|\psi^1\rangle = \langle\varphi_0^2|\varphi_0^1\rangle + O(\epsilon^2). \qquad (69)$$

By using the numerical solutions of the time-dependent, coupled, 3D GP equations, we calculate the spatial overlap $\langle\psi^2|\psi^1\rangle$ and by using the numerical solutions of Eqs. (39) and (40), we calculate the overlap $\langle\varphi_0^2|\varphi_0^1\rangle$, both as a function of time for various atom numbers. In addition, we calculate the spatial overlap between the numerical solutions of the quasi-1D, time-dependent GP equation (the reduced-dimension approximation) to use as a benchmark for our (relative-state-decomposition perturbation) model [20]. We stress that these spatial overlaps and the resulting Ramsey fringes, including those coming from the reduced-dimension approximation, are more than the simple estimates (64) and (67), since the numerical integrations include effects of position-dependent phase shifts and reduction in fringe visibility (see Sec. 5.4.3) not captured by the simple estimates of fringe frequency.

In Fig. 7, we compare the Ramsey fringes obtained from the imaginary part of

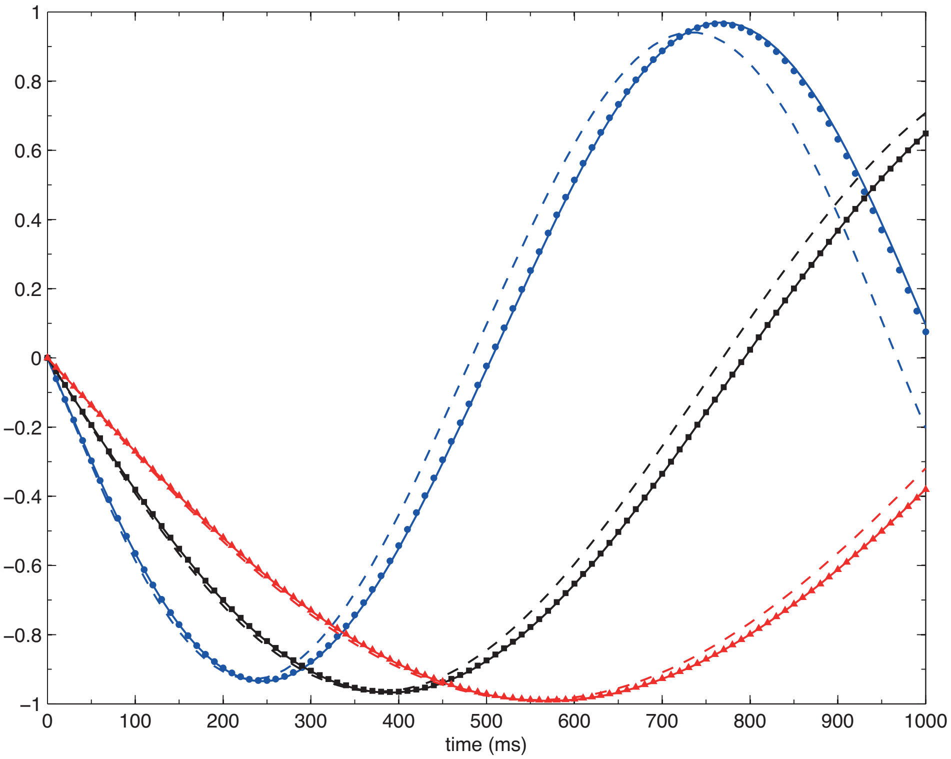

Figure 7. Ramsey fringes for a cigar-shaped ^{87}Rb BEC of 500 atoms. The points correspond to the results of the numerical integration of the time-dependent, coupled, two-mode, three-dimensional GP equations (4.22) for the different trapping potentials (4.13): circles (blue) correspond to $q = 2$, squares (black) to $q = 4$, and triangles (red) to $q = 10$. The corresponding solid lines are the numerical results of the integration of Eqs. (39) and (40), given by the relative-state-decomposition perturbation theory. The dashed lines represent the results coming from the numerical integration of the time-dependent, two-mode, quasi-1D GP equation (the reduced-dimension approximation). For all three trap geometries, the agreement between our perturbation theory and the exact 3D numerics is remarkably good during the whole 1s of integration time. The reduced-dimension approximation, on the other hand, only describes earlier stages of the evolution. As q increases, both models achieve a better performance. Note that the reduction in the fringe visibility is small, being almost absent for $q = 10$.

these three spatial overlaps for a condensate of 500 atoms. For all three longitudinal potentials, our perturbation theory reproduces the exact 3D numerics remarkably well during the entire integration time interval. The reduced-dimension approximation, on the other hand, only holds in the earliest stages of the evolution, for about a quarter of a fringe period. It is no surprise that as the traps get harder and more homogeneous, both models achieve a better performance. Note that in this case of rather small nonlinearities ($N/\mathcal{N}_T \sim 3.5 \times 10^{-2}$), the reduction in the fringe visibility due to position-dependent differential phases is quite small, being almost absent for $q = 10$. This effect becomes obvious for stronger couplings, however, as illustrated in Fig. 8 for a condensate of 1 000 atoms. For this many atoms and same time window of 1 s, the agreement between our perturbation model and the 3D solution is still quite good, especially for the more

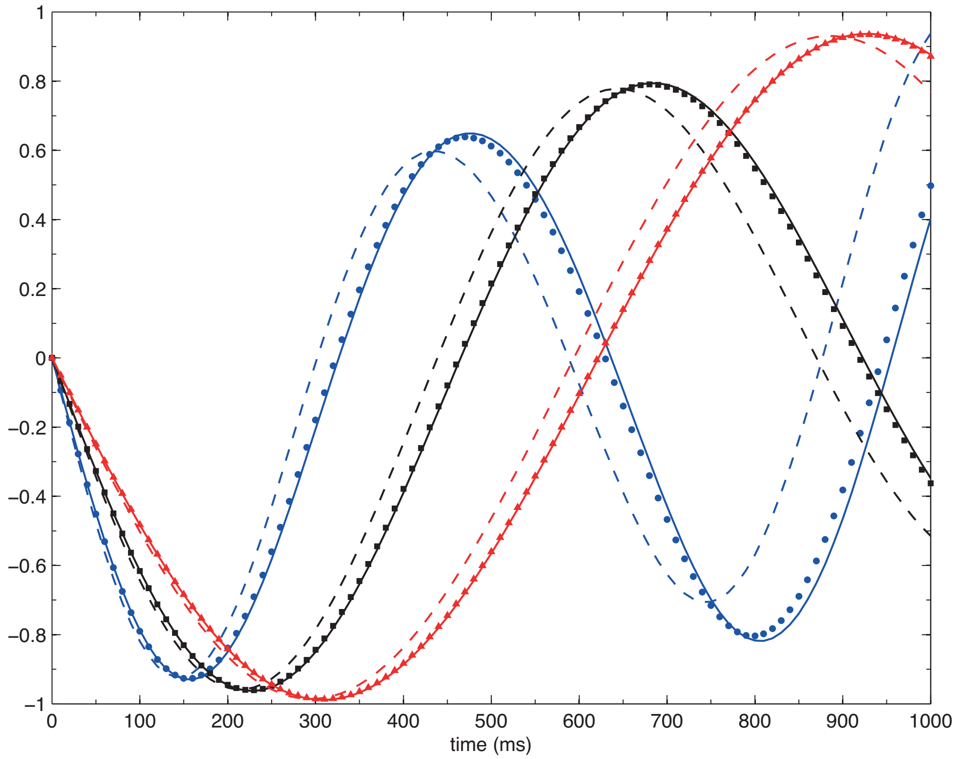

Figure 8. Ramsey fringes for a cigar-shaped ^{87}Rb BEC of 1 000 atoms (labeling convention as in Fig. 7). The points represent the numerical results of the integration of the time-dependent, coupled, two-mode 3D GP equations for the different trapping potentials (59), whereas the lines are the relative-state (solid) and quasi-1D (dashed) predictions. The agreement between our model and the 3D solution is quite good, specially for the $q = 4$ and $q = 10$ cases. Both fringe frequency and amplitude are better predicted by our model than by the reduced-dimension (quasi-1D) approximation. For $q = 2$, small deviations from the expected signal accumulate over time, resulting in a phase mismatch around $t = 500$ ms.

homogeneous trapping potentials $q = 4$ and $q = 10$. Both fringe frequency and amplitude are well predicted by our model, showing a substantial improvement over the reduced-dimension approximation. For a harmonic trap, small deviations from the expected signal accumulate over time, resulting in an evident phase mismatch around $t = 500$ ms.

For a condensate of 2 000 atoms, our model starts to break down, as shown in Fig. 9. For all q's, the reduction in fringe visibility is still well captured by our perturbative equations, with agreement with the 3D numerics getting better as q increases, but the predicted fringe frequency is a bit too small. This effect becomes more obvious for a larger condensate with 5 000 atoms. As clearly seen in Fig. 10, our prediction of the fringe frequency is too small and thus shows the complete breakdown of our perturbation model, which fails to describe the correct relative-phase accumulation.

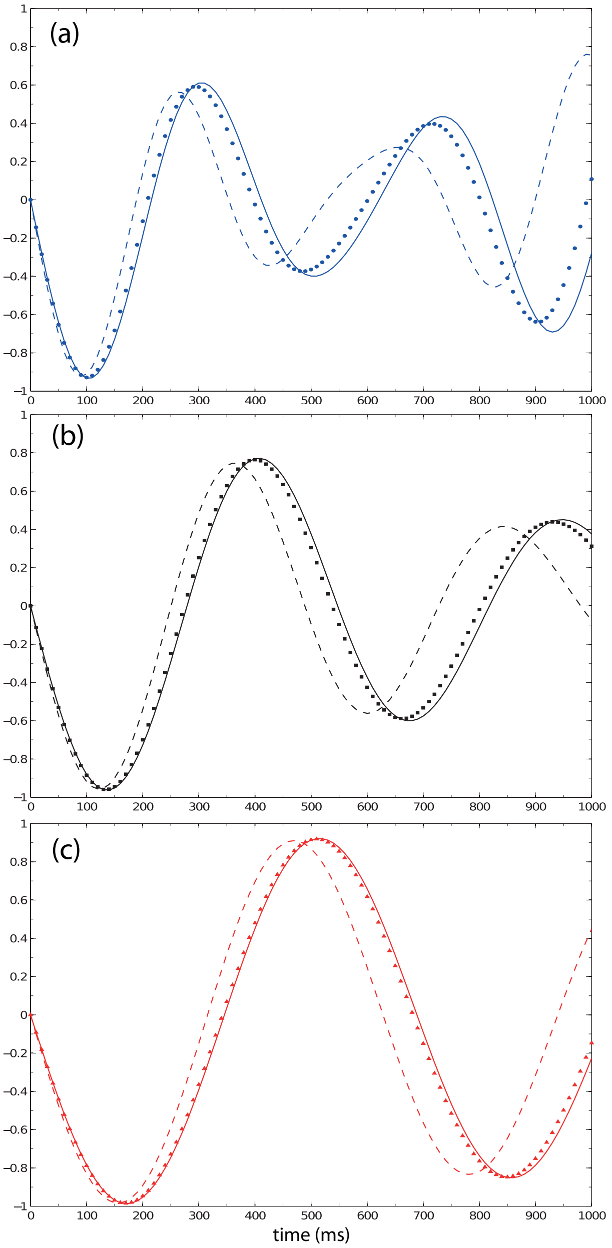

Figure 9. Ramsey fringes for a cigar-shaped ^{87}Rb BEC of 2 000 atoms trapped by the potentials (59) with (a) $q = 2$, (b) $q = 4$, (c) $q = 10$. The points represent the numerical results of the integration of the time-dependent, coupled, two-mode 3D GP equations. Solid lines are the corresponding relative-state predictions, whereas the dashed lines are results coming from the numerical solution of the quasi-1D GP equation. The reduction in fringe visibility is still well captured by our model, with agreement with the 3D numerics getting better as q increases. The predicted fringe frequency, however, is a bit too small, which points to the breakdown of the perturbation theory, yet more evident for 5 000 atoms in Fig. 10.

5.4.2. Source terms. As a brief remark, we point out that in all the results presented in this section, the solutions to Eqs. (39) and (40) take into account the source terms that arise due to the difference $\varphi_n^\alpha(0) - \tilde{\varphi}_n^\alpha(0)$. We do expect that the contribution

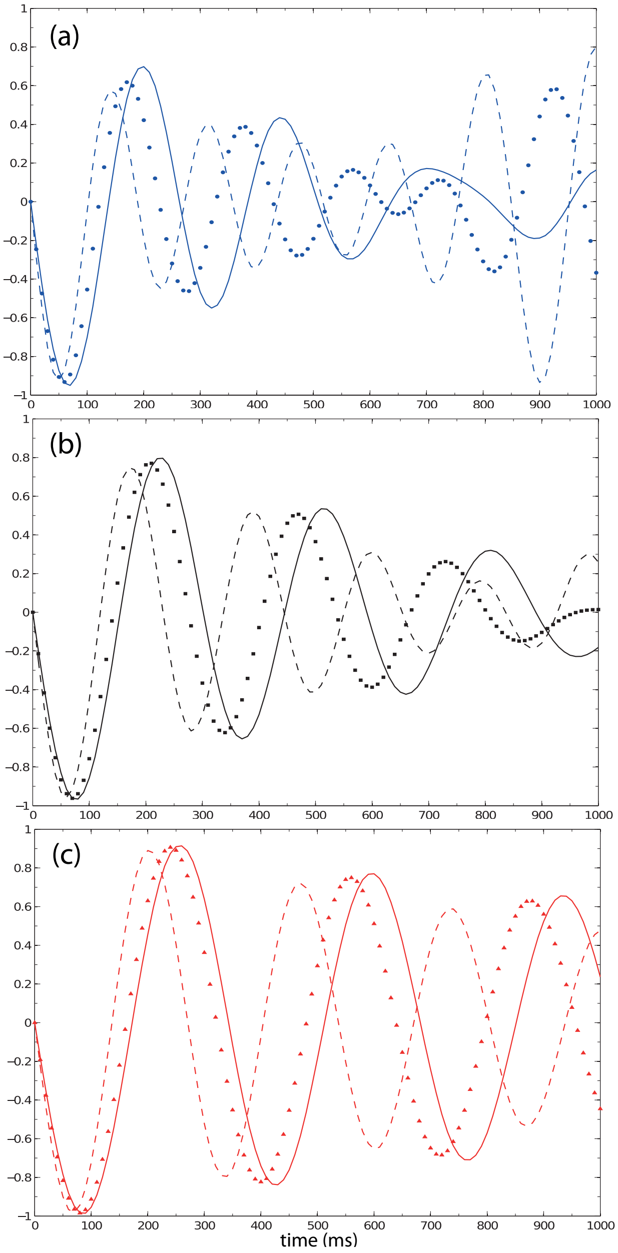

Figure 10. Ramsey fringes for a cigar-shaped ^{87}Rb BEC of 5 000 atoms trapped by the potentials (59) with (a) $q = 2$, (b) $q = 4$, (c) $q = 10$. The points represent the numerical results of the integration of the time-dependent, coupled, two-mode 3D GP equations. Solid lines are the corresponding relative-state predictions, whereas the dashed lines are results coming from the numerical solution of the quasi-1D GP equation. The perturbation theory breaks down: Eqs. (39) and (40) can no longer correctly describe the relative-phase accumulation by the condensate mean fields.

of the source terms is quite small for the initial condition we use. To verify this, we plot in Figs. 11 and 12 the predicted Ramsey fringes for 1 000 and 5 000 atoms using the solutions of Eqs. (39) and (40) with and without the contribution from the source terms. The difference in the computed overlaps is indeed quite small, being of order

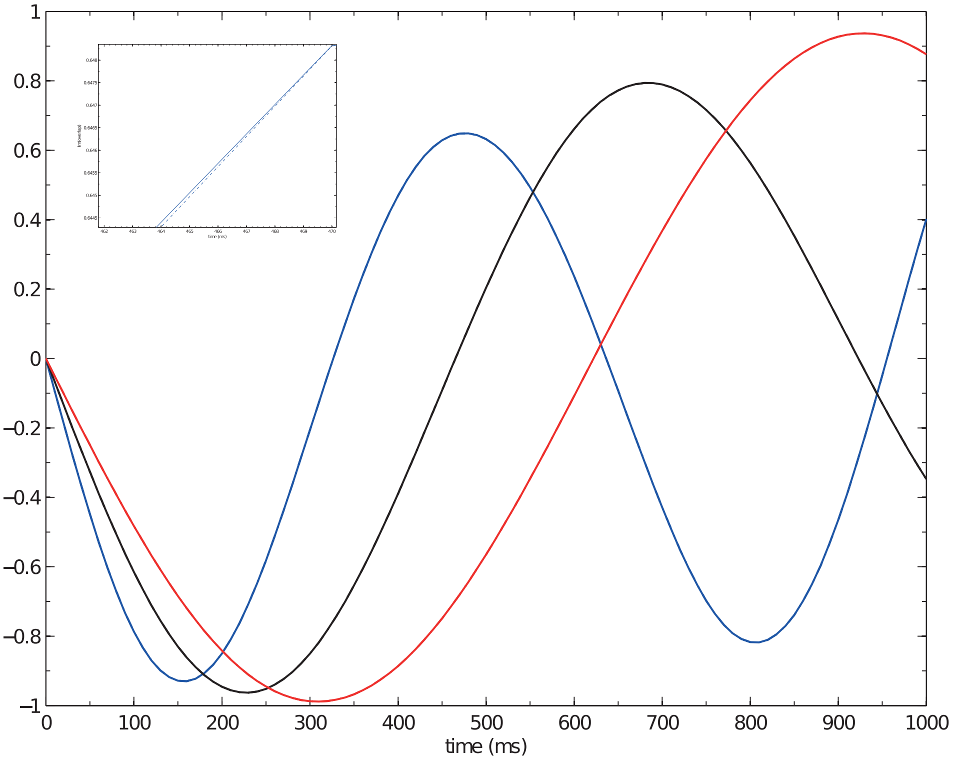

Figure 11. Ramsey fringes for 1 000 atoms using the solutions of Eqs. (39) and (40) with (solid line) and without (dash-dotted line) the contribution from the source terms for $q = 2, 4, 10$ (blue, black, red). The two lines lie almost on top of one another. The inset shows a closeup for the $q = 2$ case around $t = 465$ ms, showing a difference of the order of 10^{-4} between the two fringes.

10^{-4} for the case of 1 000 atoms and 10^{-3} for 5 000 atoms, as shown in the insets of Figs. 11 and 12 for the harmonic trap.

5.4.3. Thomas-Fermi estimates. For the traps and atom numbers that we are considering, it is legitimate to ignore the kinetic-energy term in Eqs. (39) and (40) and work in the longitudinal Thomas-Fermi approximation. Within this regime, the probability densities do not change with time, i.e.,

$$|\varphi_0^{\alpha}(z,t)|^2 = |\varphi_0(z,0)|^2, \tag{70}$$

with $|\varphi_0(z,0)|^2$ given by the Thomas-Fermi solution of Eq. (44),

$$|\varphi_0(z,0)|^2 = \frac{\tilde{\mu}_L - V_L}{\tilde{g}\eta_T} + \epsilon \frac{3\tilde{g}\Upsilon_T}{\eta_T} \left(\frac{\tilde{\mu}_L - V_L}{\tilde{g}\eta_T} \right)^2 \equiv \mathcal{Q}_0(z). \tag{71}$$

Under this approximation the two-mode evolution can be described by a simple

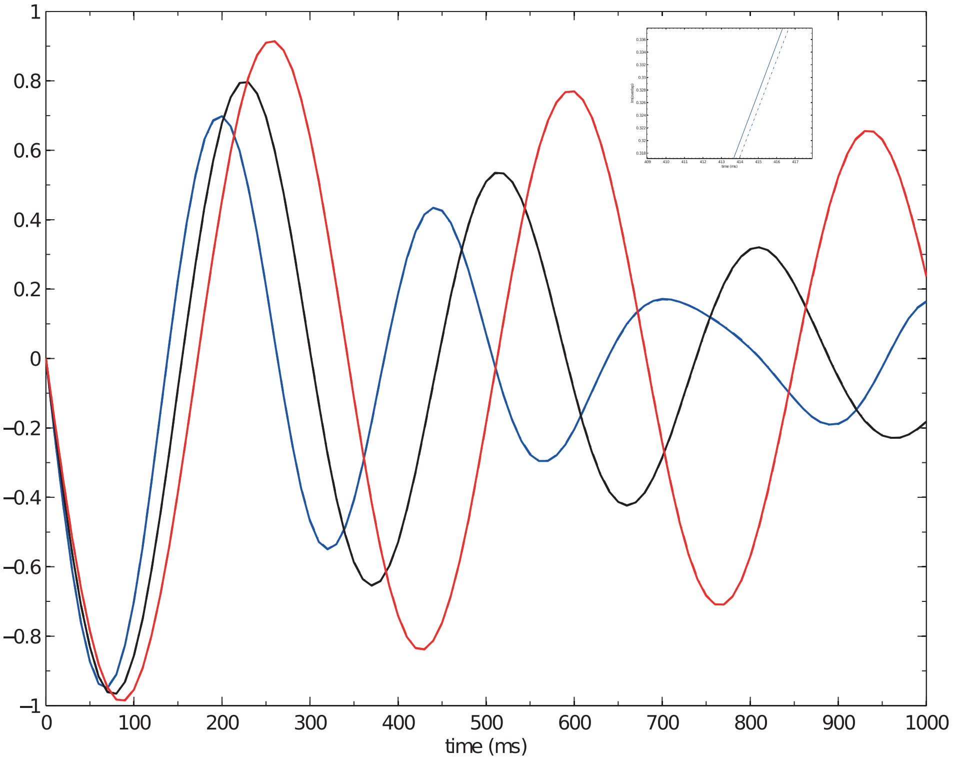

Figure 12. Ramsey fringes for 5 000 atoms using the solutions of Eqs. (39) and (40) with (solid line) and without (dash-dotted line) the contribution from the source terms for $q = 2, 4, 10$ (blue, black, red). The two lines lie almost on top of one another. The inset shows a closeup for the $q = 2$ case around $t = 415$ ms, showing a difference of the order of 10^{-3} between the two fringes.

accumulation of a phase that depends on the local atomic linear density, given by

$$\varphi_0^\alpha(z,t) = \sqrt{\mathcal{Q}_0(z)}\exp\Bigg[-\frac{it}{\hbar}\Bigg(\frac{1}{2}kz^q + \eta_T\mathcal{Q}_0(z)(\tilde{g}_{\alpha\alpha} + \tilde{g}_{\alpha\beta}) - \epsilon\Upsilon_T\mathcal{Q}_0^2(z)(3\tilde{g}_{\alpha\alpha}^2 + 3\tilde{g}_{\alpha\beta}^2 + \tilde{g}_{\alpha\beta}(4\tilde{g}_{\alpha\alpha} + 2\tilde{g}_{\beta\beta})\Bigg)\Bigg]. \tag{72}$$

This yields an overlap

$$\langle\varphi_0^2|\varphi_0^1\rangle = \int dz\,\mathcal{Q}_0(z)e^{-i\delta\theta(z)}, \tag{73}$$

where the position-dependent differential phase shift is

$$\delta\theta(z) = \frac{(N-1)\eta_T\mathcal{Q}_0(z)\gamma_1\,t}{\hbar}\left(1 - \epsilon\frac{\Upsilon_T}{\eta_T}\mathcal{Q}_0(z)(3\tilde{g}_{11} + 3\tilde{g}_{22} + 2\tilde{g}_{12})\right). \tag{74}$$

Note that we can easily retrieve the Thomas-Fermi prediction of the quasi-1D approximation by taking the limit $\epsilon \to 0$. This gives the following approximation for the overlap (62)

$$\langle\psi^2|\psi^1\rangle \approx \langle\phi^2|\phi^1\rangle = \int dz\,q_0(z)e^{-i\delta\theta(z)}, \tag{75}$$

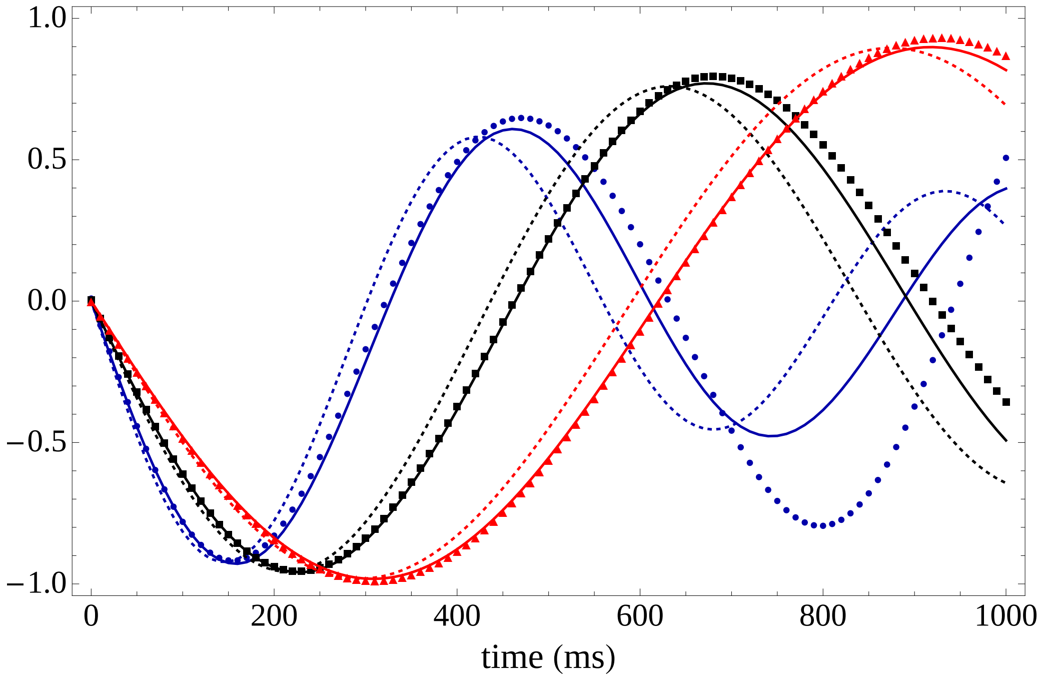

Figure 13. Same as Fig. 8 (1 000 atoms), but here the lines correspond to the Thomas-Fermi estimate (73) for $q = 2, 4, 10$ (blue, black, red). Equation (73) provides a very good account of the exact 3D fringe signal (dots), with better agreement for short times and for harder traps. For longer times, however, the analytical Thomas-Fermi model breaks down, which suggests that the probability densities can no longer be regarded as constants in time.

where the relative phase is

$$\delta\theta(z) = \frac{(N-1)\eta_T q_0(z)\gamma_1\, t}{\hbar}, \tag{76}$$

with $q_0(z)$ being given by

$$q_0(z) = \frac{\mu_L - kz^q/2}{\tilde{g}\eta_T}. \tag{77}$$

Here μ_L, the zero-order longitudinal part of the chemical potential, is determined from the normalization condition for $q_0(z)$, which gives

$$\mu_L = \frac{k}{2}\left(\frac{q+1}{q}\frac{\tilde{g}\eta_T}{k}\right)^{q/(q+1)}. \tag{78}$$

Note that, as far as the spatial overlap (73) is concerned, not only the transverse, but also the longitudinal correction play a role in rectifying the reduced-dimension approximation (75). Comparing the two overlaps, one can interpret the longitudinal correction as coming from the distribution $\mathcal{Q}_0(z)$, whereas the transverse correction comes from a rectified η_T, which is given by

$$\eta_T(z) = \eta_T - \epsilon\Upsilon_T\mathcal{Q}_0(z)(3\tilde{g}_{11} + 3\tilde{g}_{22} + 2\tilde{g}_{12}). \tag{79}$$

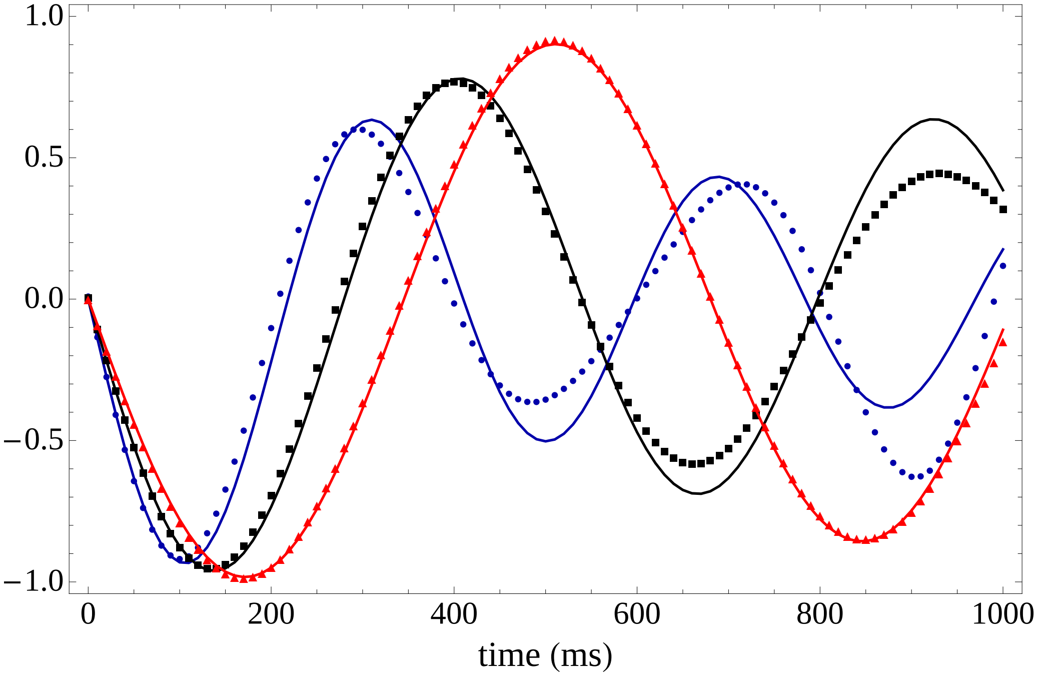

Figure 14. Same as Fig. 9 (2 000 atoms), but here the lines correspond to the Thomas-Fermi estimate (73) for $q = 2, 4, 10$ (blue, black, red). The agreement between the exact 3D overlap and Eq. (73) is still good for the harder traps $q = 4$ and $q = 10$. For $q = 10$, in particular, the mode provides the correct prediction for the entire integration time. For $q = 2$, however, the model quickly deviates from the expected 3D numerical signal (dots), due to changes in the probability densities.

Note that $\eta_T(z)$ is a function of the local axial distribution $\mathcal{Q}_0(z)$ and, hence, takes into account inhomogeneities in the trapping confinement.

In Fig. 13, we show the imaginary part of the overlap (73) for 1 000 atoms and compare it with the exact 3D overlap and the reduced-dimension prediction given by Eq. (75). The Thomas-Fermi estimate (73) provides a very good account of the exact 3D fringe signal, being far superior to the quasi-1D model. As expected, the agreement with the 3D numerics gets better for higher q and shorter times. For longer times, however, the assumption of a constant probability density is no longer valid, and the Thomas-Fermi approximation breaks down. Figure 14 shows the same comparison for 2 000 atoms, but without the ineffective quasi-1D results. For $q = 2$ and $q = 4$, deviations from the exact fringe pattern become significant after a quarter of a fringe period. For $q = 10$, however, our analytical prediction using the Thomas-Fermi approximation is remarkably accurate.

5.5. Average densities

To examine further the extent to which our perturbative approach correctly describes the two-mode evolution, we study below the dynamics of the average mean-field densities for various atom numbers. In particular, we can use the perturbation theory to describe the density evolution up to a point where the spatial separation becomes clearly apparent (see Fig. 15).

According to the perturbative expansion (6), the average single-mode density per atom, to first order in ϵ, is given by

$$\eta_\alpha(t) = \int d^3r\, |\psi^\alpha(t)|^4 \tag{80}$$

$$= \eta_T \eta_L^\alpha(t) + 2\epsilon \sum_{n=1}^{\infty} \langle \xi_n | \xi_0^3 \rangle \int dz\, |\varphi_0^\alpha(t)|^2 \big(\varphi_0^{\alpha *}(t) \varphi_n^\alpha(t) + \text{c.c.} \big), \tag{81}$$

where

$$\eta_L^\alpha(t) = \int dz\, |\varphi_0^\alpha(t)|^4. \tag{82}$$

Within the adiabatic approximation (20) to $\varphi_n^\alpha(t)$, we can split Eq. (81) into two terms, a dominant term and a second term that comes from the source term in Eq. (20):

$$\eta_\alpha(t) = \tilde{\eta}_\alpha(t) + \tilde{\eta}_I^\alpha(t). \tag{83}$$

The dominant term, which is given by

$$\tilde{\eta}_\alpha(t) = \eta_T \eta_L^\alpha(t) + 2\epsilon \sum_{n=1}^{\infty} \langle \xi_n | \xi_0^3 \rangle \int dz\, |\varphi_0^\alpha(t)|^2 \big(\varphi_0^{\alpha *}(t) \tilde{\varphi}_n^\alpha(t) + \text{c.c.} \big), \tag{84}$$

includes the contributions that arise from φ_0^α and $\tilde{\varphi}_n^\alpha$. By using Eq. (21) and introducing the quantities

$$\eta_{L6}^\alpha(t) = \int dz\, |\varphi_0^\alpha(t)|^6, \tag{85}$$

$$\eta_L^{\alpha\alpha\beta}(t) = \int dz\, |\varphi_0^\alpha(t)|^4 |\varphi_0^\beta(t)|^2, \tag{86}$$

we can write the dominant term in the more compact form

$$\tilde{\eta}_\alpha(t) = \eta_T \eta_L^\alpha(t) - 4\epsilon \Upsilon_T \left(\tilde{g}_{\alpha\alpha} \eta_{L6}^\alpha(t) + \tilde{g}_{\alpha\beta} \eta_L^{\alpha\alpha\beta}(t) \right). \tag{87}$$

The second term in Eq. (83),

$$\tilde{\eta}_I^\alpha(t) = 2\epsilon \sum_{n=1}^{\infty} \langle \xi_n | \xi_0^3 \rangle \int dz\, |\varphi_0^\alpha(t)|^2 \big(\varphi_0^{\alpha *}(t) \tilde{I}_n^\alpha(t) + \text{c.c.} \big), \tag{88}$$

comes from the source term $\tilde{I}_n^\alpha$. Together with Eqs. (57) and (58), this gives

$$\tilde{\eta}_I^1(t) = -4\epsilon \gamma_1 (N-1) \int dz\, \varphi_{00}^3 |\varphi_0^1(t)|^2 \Big(\varphi_0^{1*}(t) \upsilon_T(t) + \text{c.c.} \Big), \tag{89}$$

$$\tilde{\eta}_I^2(t) = -6\epsilon \gamma_1 (N-1) \int dz\, \varphi_{00}^3 |\varphi_0^2(t)|^2 \Big(\varphi_0^{2*}(t) \upsilon_T(t) + \text{c.c.} \Big). \tag{90}$$

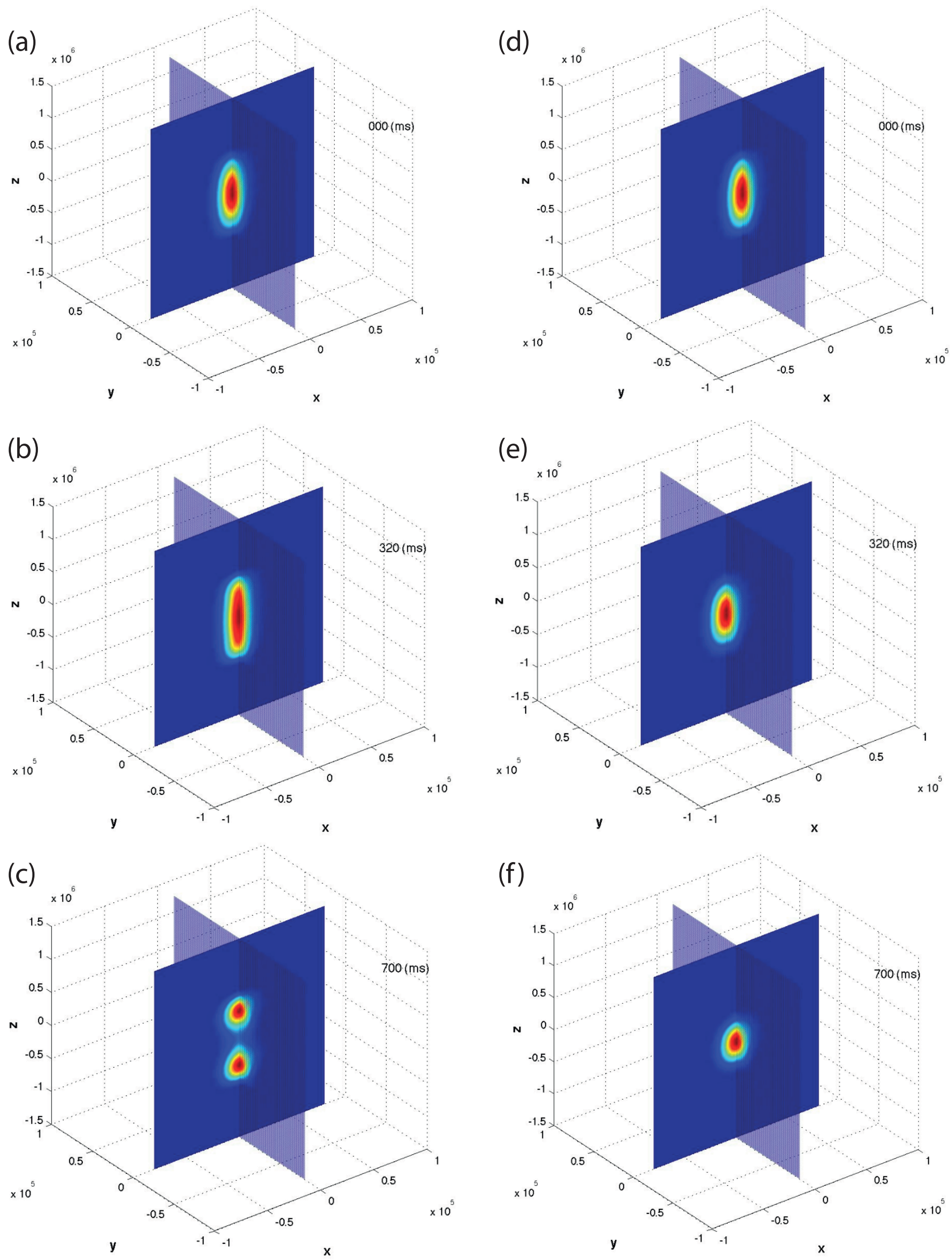

Figure 15. Density evolution for a BEC of 1 000 atoms and $q = 2$. The subplots on the left show the time evolution of $|\psi^1(\rho, z, t)|^2$, whereas the time evolution of $|\psi^2(\rho, z, t)|^2$ is illustrated by the figures on the right. Initially, both modes have the same density profile as seen in subplots (a) and (d). The position-dependent phases acquired by each mode drive differences between the atomic densities associated with the two hyperfine levels, as seen in subplots (b) and (e) for 320 ms of evolution. Atoms in mode 1 are pushed towards the edges of the trap due to the stronger intra-mode repulsion ($g_{11} > g_{12} > g_{22}$), while atoms in mode 2 get compressed in the center of trap by the atoms in mode 1 because of the inter-mode repulsion ($g_{12} > g_{22}$). This leads to spatial separation of the two modes, as shown in subplots (c) and (f) at 700 ms of the evolution. Due to the trap confinement, this dynamics is eventually reversed. The dynamical relative-state perturbation theory allows us to investigate the density evolution long enough to capture all of these effects.

A similar set of steps, using Eqs. (6) and (20), splits the density overlap,

$$\eta_{12}(t) = \int d^3r\, |\psi^1(t)|^2 |\psi^2(t)|^2, \tag{91}$$

into two terms,

$$\eta_{12}(t) = \tilde{\eta}_{12}(t) + \tilde{\eta}_I^{12}(t), \tag{92}$$

where

$$\tilde{\eta}_{12}(t) = \eta_T \eta_L^{12}(t) - 2\epsilon \Upsilon_T [(\tilde{g}_{11} + \tilde{g}_{12})\eta_L^{112}(t) + (\tilde{g}_{22} + \tilde{g}_{12})\eta_L^{221}(t)], \tag{93}$$

$$\eta_L^{12}(t) = \int dz\, |\varphi_0^1(t)|^2 |\varphi_0^2(t)|^2, \tag{94}$$

and

$$\begin{aligned} \tilde{\eta}_I^{12}(t) = &-3\epsilon\gamma_1(N-1) \int dz\, \varphi_{00}^3 |\varphi_0^1(t)|^2 \Big(\varphi_0^{2*}(t)\upsilon_T(t) + \text{c.c.}\Big) \\ &- 2\epsilon\gamma_1(N-1) \int dz\, \varphi_{00}^3 |\varphi_0^2(t)|^2 \Big(\varphi_0^{1*}(t)\upsilon_T(t) + \text{c.c.}\Big). \end{aligned} \tag{95}$$

Our first step in studying the time evolution of the mean-field densities is simply to calculate $\eta_1(t)$, $\eta_2(t)$, and $\eta_{12}(t)$, as instructed by Eqs. (80) and (91), using the numerical solutions of the time-dependent 3D GP equation (5). We compare these to the relative-state predictions (83) and (92). Again, we also calculate the corresponding predictions of the reduced-dimension approximation to use as a benchmark to our model. Figures 16, 17, and 18 show these three quantities in harmonic trap units [21] for $q = 2, 4$ and 10. In each figure, we consider the cases for 500, 1 000, 2 000, and 5 000 atoms. We note that the 3D numerical solutions, the relative-state model, and the reduced-dimension approximation all use different initial conditions.

In all cases, we can see that the 3D mean densities are poorly described by the reduced-dimension approximation. Our perturbative model, however, manages to reproduce the exact mean densities remarkably well for 500 and 1 000 atoms. Small deviations appear for 2 000 atoms; for 5 000 atoms, the model gives entirely incorrect predictions for the density evolution. The case $q = 10$ and $N = 500$ is an exception to the previous statement. For this particular case, numerical instabilities affected the calculation of the initial longitudinal wave functions $\varphi_0^1(0)$ and $\varphi_0^2(0)$, which consequently resulted in the inaccurate density dynamics seen in Fig. 18(a). Note, however, that this numerical error does not seem to affect the good agreement for the relative phases shown in Fig. 7.

The two-mode density evolution shown in Figs. 16–18 can roughly be described as follows. Initially all densities are the same, i.e., $\eta_1(0) = \eta_2(0) = \eta_{12}(0)$; hence, the earlier stage of the dynamics is essentially dictated by the different scattering couplings. Thus, atoms in mode 1 are initially pushed towards the edges of the trap due to the stronger

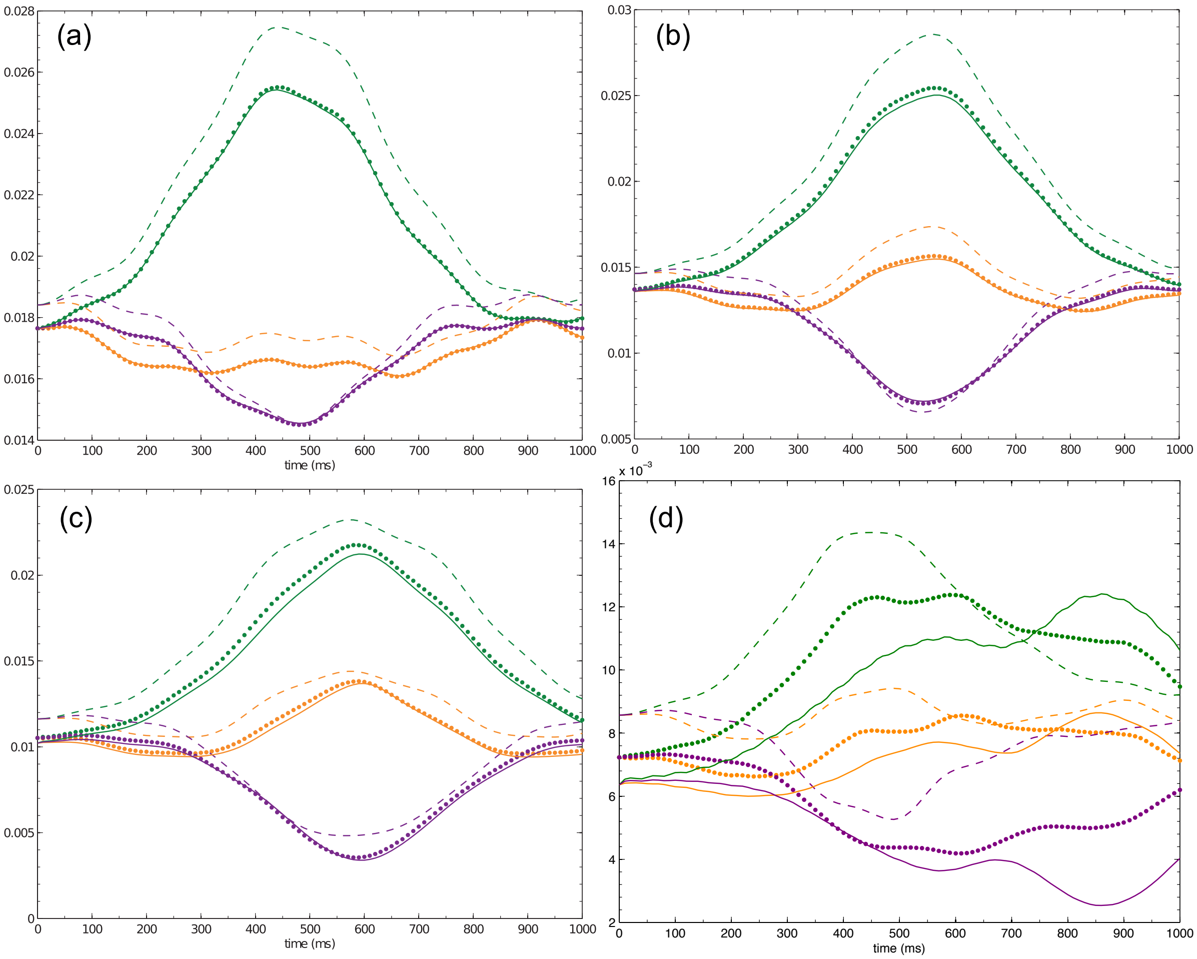

Figure 16. Time evolution of the average densities, η_1 (orange) and η_2 (green), and of the density overlap, η_{12} (purple), for $q = 2$ and (a) $N = 500$, (b) $N = 1\,000$, (c) $N = 2\,000$, and (d) $N = 5\,000$. The points represent the numerical results of the integration of the time-dependent, coupled, two-mode 3D GP equations. Solid lines are the respective relative-state predictions, whereas the dashed lines are results coming from the numerical solution of the quasi-1D GP equation (reduced-dimension approximation). In all cases, the 3D mean densities are poorly described by the reduced-dimension approximation. Our perturbative model, on the other hand, performs extremely well, except for $N = 5\,000$, where the model breaks down.

intra-mode repulsion ($g_{11} > g_{12} > g_{22}$), while atoms in mode 2 get compressed in the center of trap by the atoms in mode 1 because of the inter-mode repulsion ($g_{12} > g_{22}$). Therefore, the wave function for mode 1 gets wider than the wave function of the second mode. In other words, the mean atomic density η_1 decreases while η_2 increases, and as the two modes are driven apart, the density overlap η_{12} drops. Of course, the atomic repulsion is counterbalanced by the trapping potential, so at some point this dynamics is reversed.

The complex nonlinear evolution in Figs. 16–18 makes it challenging to analyze further the dynamical behavior of the mean-field densities. To gain a deeper understanding of the results, we examine the renormalized single-mode mean densities,

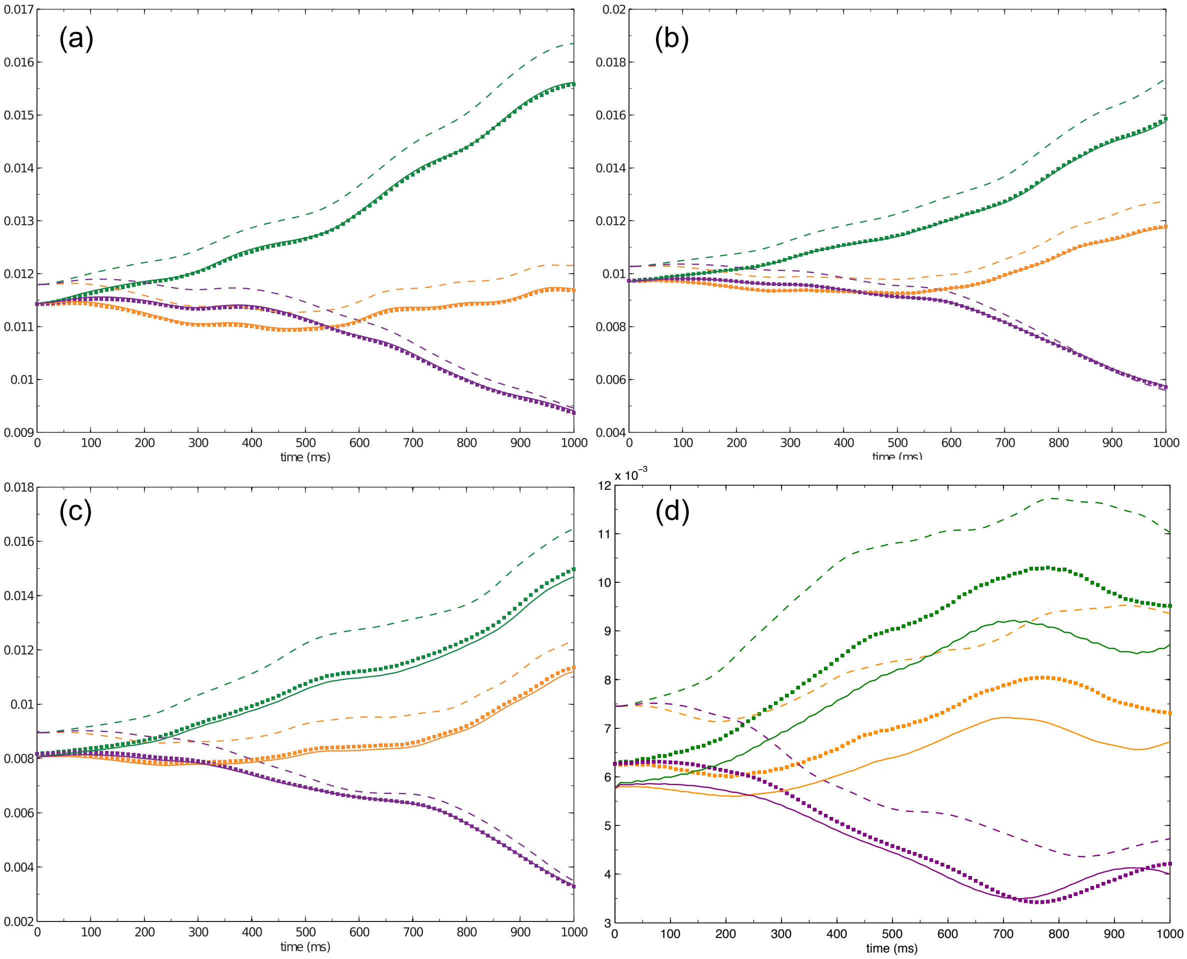

Figure 17. Time evolution of the average densities, η_1 (orange) and η_2 (green), and of the density overlap, η_{12} (purple), for $q = 4$ and (a) $N = 500$, (b) $N = 1\,000$, (c) $N = 2\,000$, and (d) $N = 5\,000$. The points represent the numerical results of the integration of the time-dependent, coupled, two-mode 3D GP equations. Solid lines are the respective relative-state predictions, whereas the dashed lines are results coming from the numerical solution of the quasi-1D GP equation. Our perturbative model performs extremely in all cases, except for $N = 5\,000$, when the model breaks down. Note that for $2\,000$ atoms, small deviations appear. The reduced-dimension approximation fails to describe the 3D mean densities in all cases.

$\bar{\eta}_1$ and $\bar{\eta}_2$, which we define according to

$$\bar{\eta}_\alpha = \frac{\eta_\alpha}{\bar{\eta}}, \tag{96}$$

where

$$\bar{\eta} = \frac{\eta_1 + \eta_2}{2} \tag{97}$$

is the arithmetic mean of the two average densities.

Figures 19, 20, and 21 show the time evolution of $\bar{\eta}_1$ and $\bar{\eta}_2$ for $q = 2, 4$, and 10. In each figure, we plot the cases $N = 500$, $1\,000$, $2\,000$, and $5\,000$. The time evolution of $\bar{\eta}_1$ and $\bar{\eta}_2$ is, in fact, much simpler than of η_1 and η_2, and, therefore, easier to interpret.

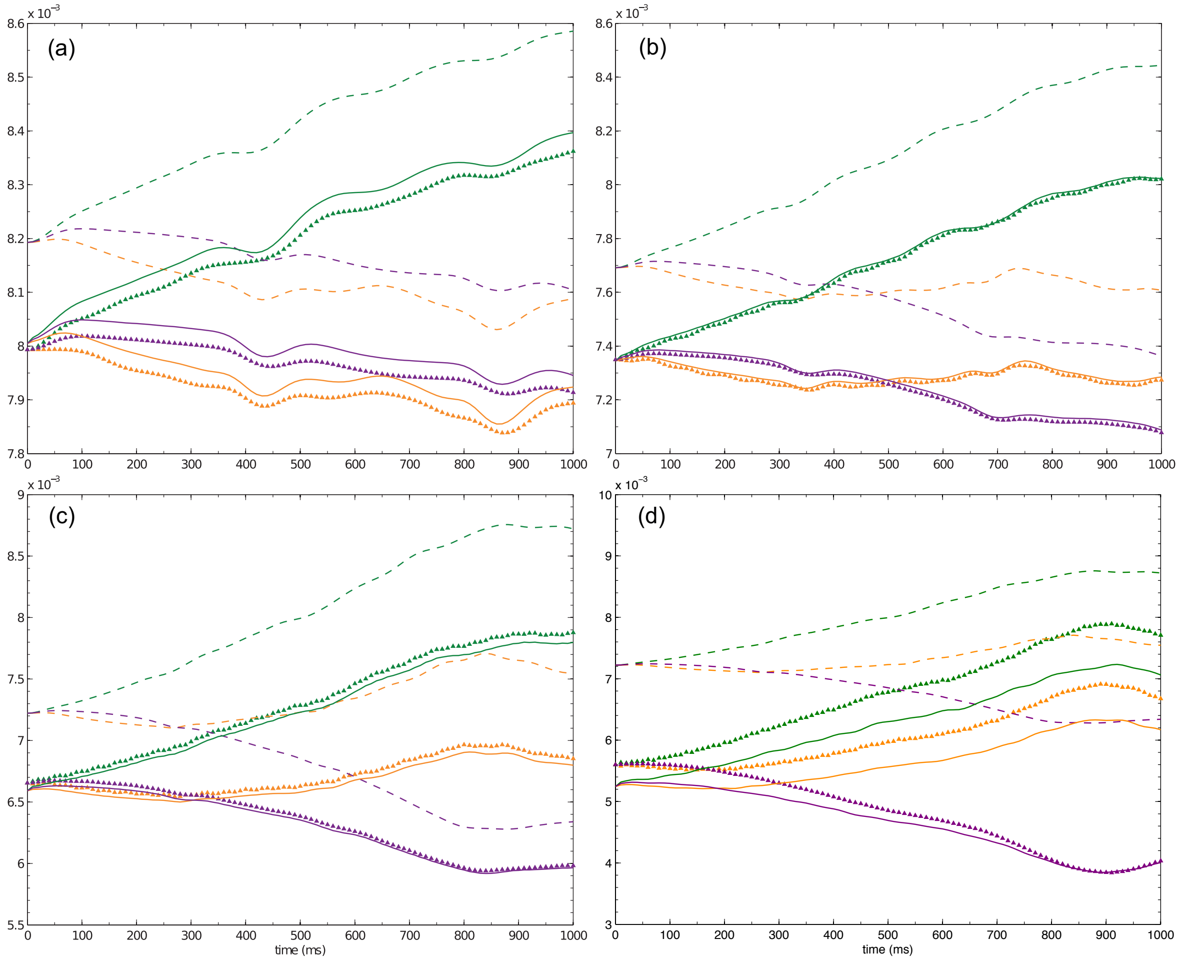

Figure 18. Time evolution of the average densities, η_1 (orange) and η_2 (green), and of the density overlap, η_{12} (purple), for $q = 10$ and (a) $N = 500$, (b) $N = 1\,000$, (c) $N = 2\,000$, and (d) $N = 5\,000$. The points represent the numerical results of the integration of the time-dependent, coupled, two-mode 3D GP equations. Solid lines are the respective relative-state predictions, whereas the dashed lines are results coming from the numerical solution of the quasi-1D GP equation. The inaccurate density dynamics seen in subplot (a) is due to numerical instabilities that affected the calculation of the initial longitudinal wave functions $\varphi_0^1(0)$ and $\varphi_0^2(0)$. This numerical error, however, does not seem to affect the good agreement for the relative phases shown in Fig. 7.

Among other things, using the renormalized average densities reduces the effect of the differences in initial conditions seen in Figs. 16–18. For instance, it is easy to see in Figs. 19–21 both the symmetry in the relative dynamics of the two modes and the suppression of the spreading of the condensate wave function with increasing q. Indeed, note that the harder the trap, the closer $\bar{\eta}_1$ and $\bar{\eta}_2$ get to 1.

More importantly, the comparison of the dynamics of η_α with of $\bar{\eta}_\alpha$ reveals an interesting fact about the dynamics of our model. The results for the renormalized average densities are clearly better described by our model than the evolution of η_1 and η_2. The cases of a condensate with $5\,000$ atoms, shown in subplot (d) of Figs. 16–18, is

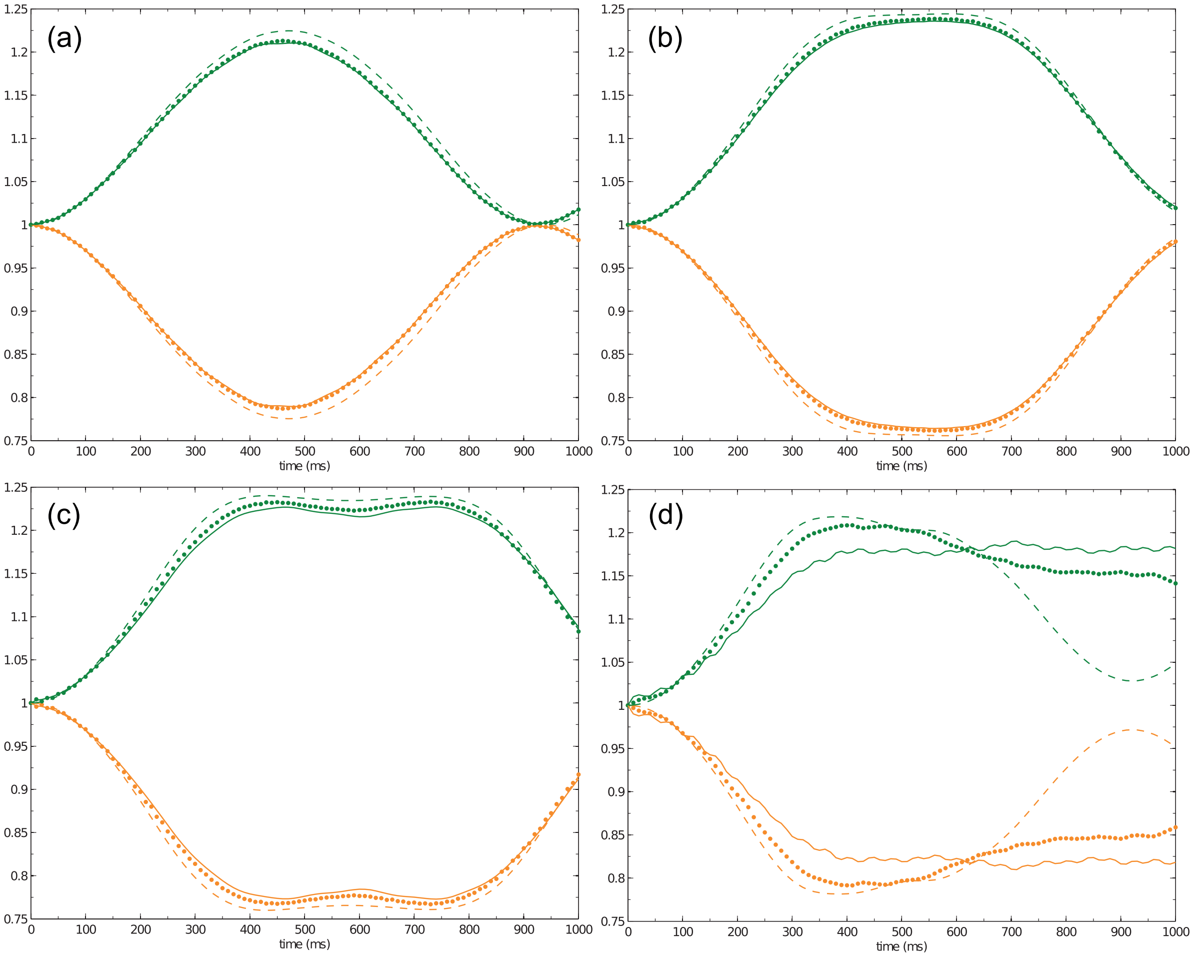

Figure 19. Time evolution of the renormalized average densities, $\bar{\eta}_1$ (orange) and $\bar{\eta}_2$ (green), for $q = 2$ and (a) $N = 500$, (b) $N = 1\,000$, (c) $N = 2\,000$, and (d) $N = 5\,000$. The points represent the numerical results of the integration of the time-dependent, coupled, two-mode 3D GP equations. Solid lines are the respective relative-state predictions, whereas the dashed lines are results coming from the numerical solution of the quasi-1D GP equation.

a good example of what we mean. In these three cases, our model failed to predict the correct density evolution. When we analyze the renormalized densities in subplot (d) of Figs. 19–21, however, this is clearly no longer the case. The agreement between the exact 3D results and our perturbation model is overall reasonably good, and it gets better for shorter times and harder traps, as is to be expected. Surprisingly, the same can also be said for the reduced-dimension predictions, for there is a dramatic improvement in the agreement between the 3D exact dynamics and the quasi-1D model. In fact, the reduced-dimension approximation failed in all the cases shown in Figs. 16–18. Figures 19–21, on the other hand, show that the evolution of $\bar{\eta}_1$ and $\bar{\eta}_2$ can be well described by the quasi-1D GP equation, specially for smaller atom numbers. These results are indeed very revealing, for they clearly indicate that Eqs. (39) and (40) predict, to some extent, the correct relative density dynamics in spite of the use of an imprecise initial condition,

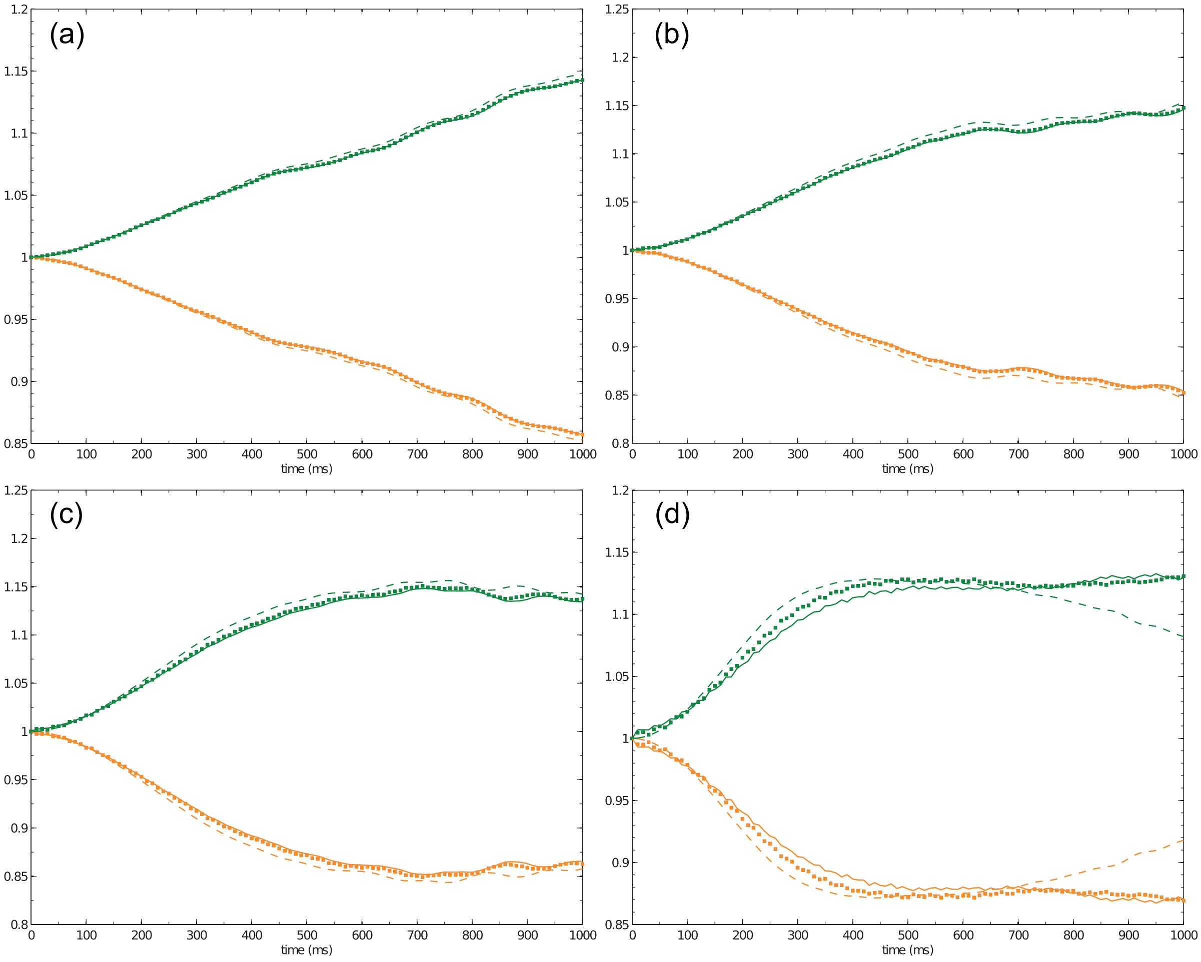

Figure 20. Time evolution of the renormalized average densities, $\bar{\eta}_1$ (orange) and $\bar{\eta}_2$ (green), for $q = 4$ and (a) $N = 500$, (b) $N = 1\,000$, (c) $N = 2\,000$, and (d) $N = 5\,000$. The points represent the numerical results of the integration of the time-dependent, coupled, two-mode 3D GP equations. Solid lines are the respective relative-state predictions, whereas the dashed lines are results coming from the numerical solution of the quasi-1D GP equation.

which is ultimately related to underestimating the transverse profile of the condensate.

Finally, we introduce the renormalized density overlap, $\mathcal{F}_\eta$, as the ratio of η_{12} to the geometric mean of the single-mode average densities, i.e.,

$$\mathcal{F}_\eta = \frac{\eta_{12}}{\sqrt{\eta_1 \eta_2}}. \tag{98}$$

This quantity is equal to zero if there is no overlap between the mean-field distributions and is equal to one when they completely overlap, thus working analogously to the fidelity of quantum states. Figure 22 shows the time evolution of Eq. (98) for $N = 500$, $1\,000$, $2\,000$, and $5\,000$ and the three different traps $q = 2, 4$ and 10. This figure nicely shows the time scale on which the condensate density is constant, which increases as the trap gets harder, as expected. During this time interval, the two-mode dynamics simply

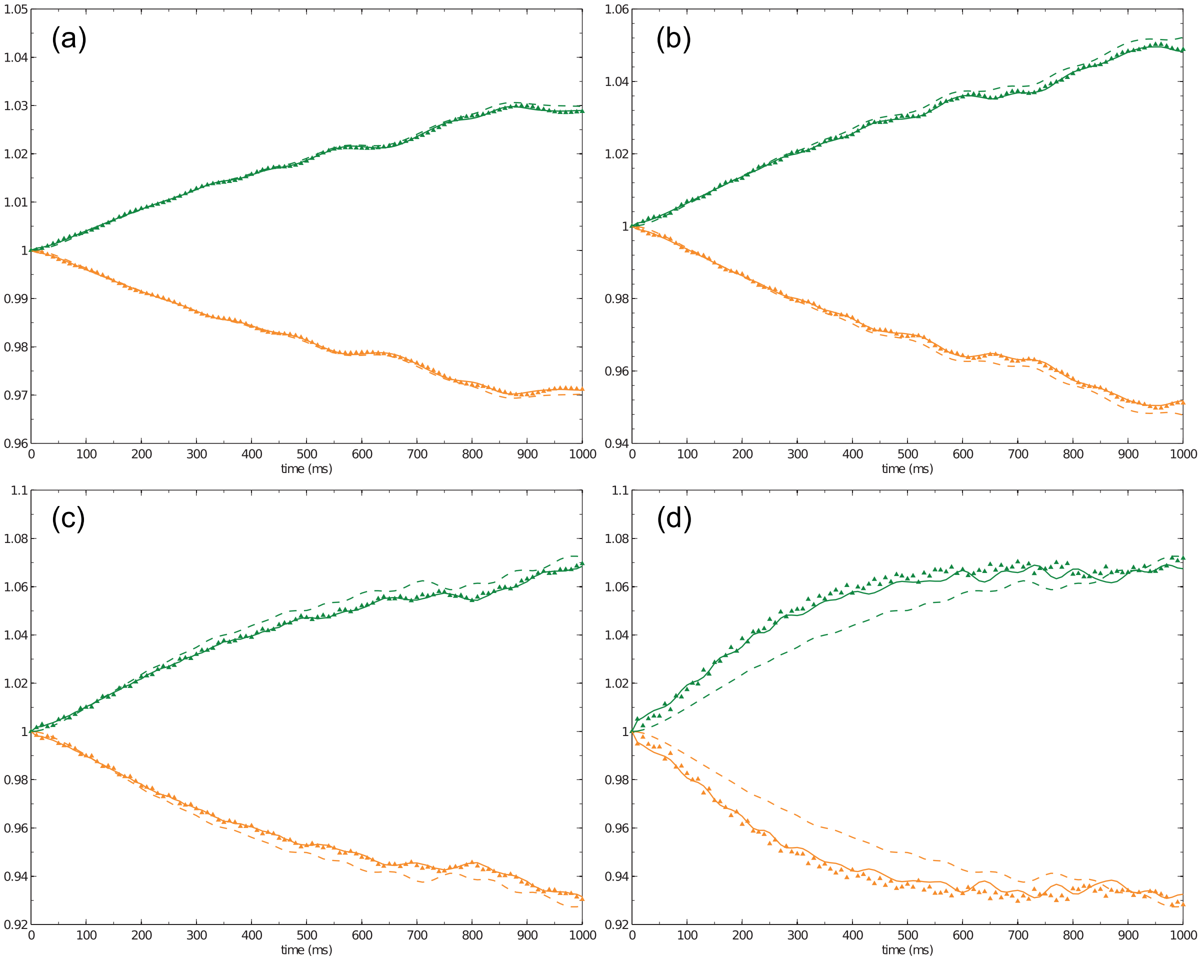

Figure 21. Time evolution of the renormalized average densities, $\bar{\eta}_1$ (orange) and $\bar{\eta}_2$ (green), for $q = 10$ and (a) $N = 500$, (b) $N = 1\,000$, (c) $N = 2\,000$, and (d) $N = 5\,000$. The points represent the numerical results of the integration of the time-dependent, coupled, two-mode 3D GP equations. Solid lines are the respective relative-state predictions, whereas the dashed lines are results coming from the numerical solution of the quasi-1D GP equation.

correspond to the accumulation of a position-dependent phase-shift. In addition, the agreement between our model and the 3D numerics is very good for the entire integration time, except for 5 000 atoms, where we see the model breaking down around 200 ms. This result enforces our previous conclusion that Eqs. (39) and (40) predict to some extent the correct relative density dynamics in spite of the use of an incorrect initial condition.

6. Optimal reduced-dimension equations for the two-mode evolution

Having successfully obtained a perturbative description of the time-dependent mean fields of the two-mode BEC, we turn now to the question of how to decouple the tightly confined dimensions from the mean-field evolution.

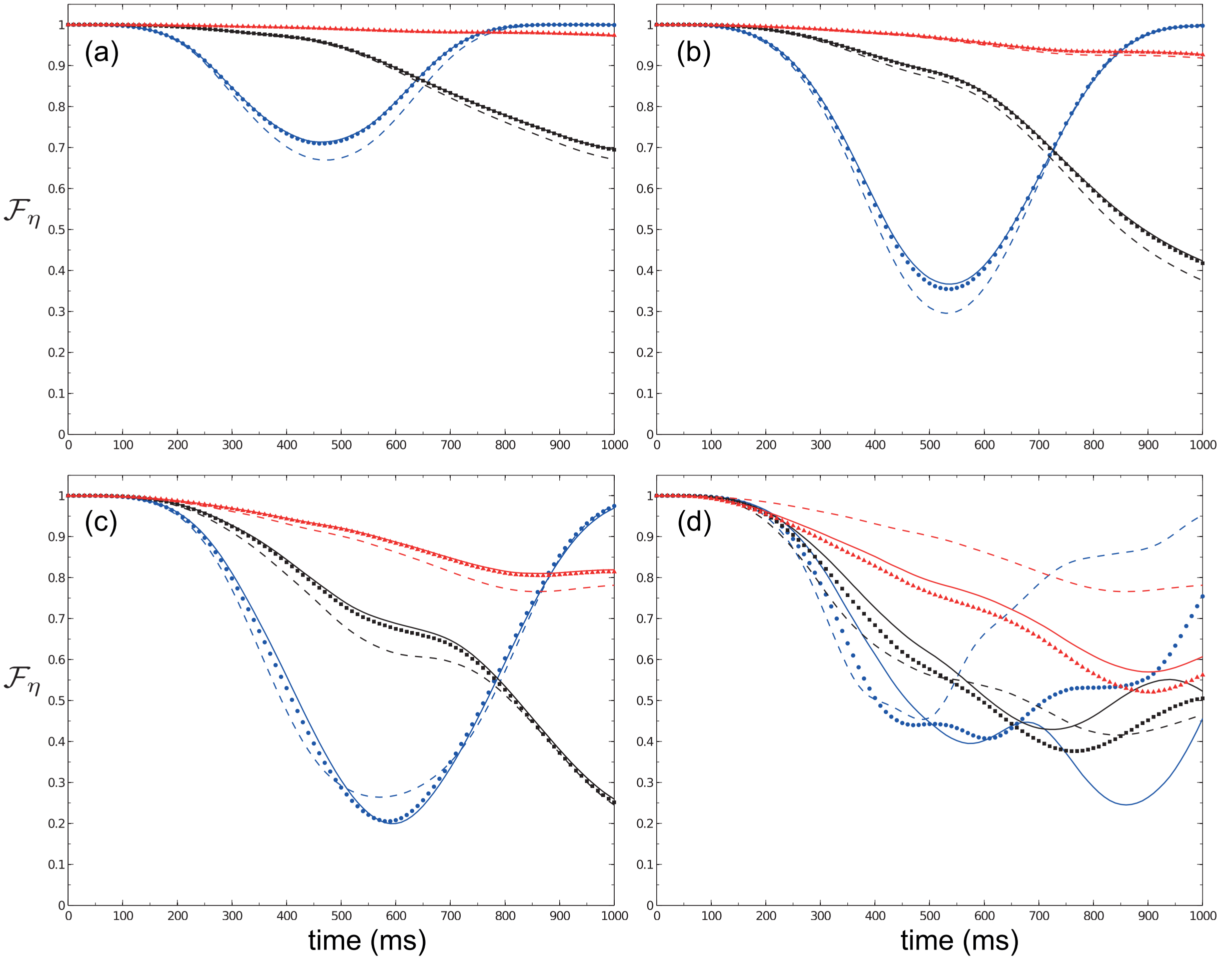

Figure 22. Time evolution of $\mathcal{F}_\eta = \eta_{12}/\sqrt{\eta_1\eta_2}$ for (a) $N = 500$, (b) $N = 1\,000$, (c) $N = 2\,000$, and (d) $N = 5\,000$ and the three different traps $q = 2, 4$, and 10 (blue, black, and red). This quantity is zero when there is no spatial overlap between the mean-field densities and is equal to one when they completely overlap. The points represent the numerical results of the integration of the time-dependent, coupled, two-mode 3D GP equations. Solid lines are the respective relative-state predictions, whereas the dashed lines are results coming from the numerical solution of the quasi-1D GP equation. The agreement between our model and the 3D numerics is very good for the entire integration time, except for 5 000 atoms, where we see the modeling breaking down around 200 ms.

For a single-mode BEC, we showed in [8] that, in the stationary case, such a decoupling can be formally achieved by performing a perturbative Schmidt decomposition of the ground-state condensate wave function, $\psi(\boldsymbol{\rho}, \boldsymbol{r})$, between the transverse and the longitudinal directions. In the Schmidt perturbation theory, we seek a solution to the time-independent, single-mode GP equation in the form

$$\psi(\boldsymbol{\rho}, \boldsymbol{r}) = \sqrt{\lambda_0}\chi_0(\boldsymbol{\rho})\phi_0(\boldsymbol{r}) + \epsilon\sqrt{\lambda_1}\chi_1(\boldsymbol{\rho})\phi_1(\boldsymbol{r}) + O(\epsilon^2), \tag{99}$$

where $\chi_n(\boldsymbol{\rho})$ and $\phi_n(\boldsymbol{r})$ are the orthonormal Schmidt functions in the transverse and longitudinal directions and the $\sqrt{\lambda_n}$'s are the (nonnegative) Schmidt coefficients (the squares λ_n are the eigenvalues of the marginal transverse and longitudinal density matrices) [23]. Note that we treat the Schmidt decomposition formally as a power-series expansion in the perturbation parameter ϵ. Thus, the dominant term in Eq. (99) gives the best product approximation to the exact condensate wave function [22], whereas the remaining terms introduce nonseparable corrections and, hence, describe entanglement between the transverse and longitudinal degrees of freedom. Because in the perturbative regime the spatial entanglement is small [8], one can neglect the nonseparable terms and describe the condensate by a product wave function. In this way, the transverse and longitudinal directions are decoupled and the dominant longitudinal Schmidt function gives the optimal reduced-dimension description for the condensate mean fields. Below we extend this formalism to the time-dependent mean fields of the two-component BEC, by showing that the instantaneous perturbative Schmidt decomposition can be obtained from the relative-state decomposition (6).

In the single-mode case, the mean field (99) has the form of a two-qubit state to first order in ϵ. In the two-mode case, however, the single-particle condensate state has the following form

$$\langle \boldsymbol{\rho}, \boldsymbol{r} | \Psi_{12}(t)\rangle = \left[\psi^1(\boldsymbol{\rho}, \boldsymbol{r}, t)|1\rangle + \psi^2(\boldsymbol{\rho}, \boldsymbol{r}, t)|2\rangle\right]/\sqrt{2}, \tag{100}$$

which corresponds to a tripartite state, for it has an additional qubit degree of freedom, namely, the two possible hyperfine configurations. Because the Schmidt decomposition only applies to bipartite systems, the decomposition of tripartite states is not unique and depends on the specific way one chooses to partition the system.

From all possible bipartitions, the one that is physically relevant for understanding the reduced-dimension structure of the mean field of a highly anisotropic condensate is the one that separates the transverse degrees of freedom from the longitudinal and hyperfine (internal) degrees of freedom. This partition relies on the physical difference between the high energy scale of the tightly confined dimensions and the much lower energy scale of the longitudinal and hyperfine degrees of freedom.

The procedure we describe next is very similar to the one discussed in [8]. We start by pointing out that the two-mode, single-particle state (100) can be written in the form of the spinor

$$\vec{\Psi}_{12} = \frac{1}{\sqrt{2}}\begin{pmatrix}\psi^1\\ \psi^2\end{pmatrix}, \tag{101}$$

which represents a vector in the two-dimensional hyperfine space, whose components are the condensate wave functions

$$\psi^\alpha = e^{-iE_0t/\hbar}\left(\xi_0\varphi_0^\alpha + \epsilon\sum_{n=1}^{\infty}\xi_n\varphi_n^\alpha\right), \tag{102}$$

and which satisfies the normalization condition,

$$\langle\vec{\Psi}_{12}|\vec{\Psi}_{12}\rangle = \frac{1}{2}\left(\langle\psi^1|\psi^1\rangle + \langle\psi^2|\psi^2\rangle\right) = 1 + O(\epsilon^2). \tag{103}$$

For simplicity, from here on we remove the initial-condition terms from our equations by assuming that $\varphi_n^\alpha(0) = \tilde{\varphi}_n^\alpha(0)$, which implies that $\varphi_n^\alpha = \tilde{\varphi}_n^\alpha$ holds at all times.

We now move toward a Schmidt decomposition by separating out the transverse degrees of freedom from the other ones in Eq. (101),

$$\vec{\psi}_{12} = \zeta_0 \vec{\varphi}_0 + \epsilon \zeta_1 \vec{\varphi}_1, \tag{104}$$

where

$$\zeta_0 = \xi_0 e^{-iE_0 t/\hbar}, \tag{105}$$

$$\zeta_1 = -e^{-iE_0 t/\hbar} \sum_{n=1}^{\infty} \xi_n \frac{\langle \xi_n | \xi_0^3 \rangle}{E_n - E_0}, \tag{106}$$

and

$$\vec{\varphi}_0 = \frac{1}{\sqrt{2}} \begin{pmatrix} \varphi_0^1 \\ \varphi_0^2 \end{pmatrix}, \tag{107}$$

$$\vec{\varphi}_1 = \frac{1}{\sqrt{2}} \begin{pmatrix} \left(\tilde{g}_{11} |\varphi_0^1|^2 + \tilde{g}_{12} |\varphi_0^2|^2\right) \varphi_0^1 \\ \left(\tilde{g}_{22} |\varphi_0^2|^2 + \tilde{g}_{12} |\varphi_0^1|^2\right) \varphi_0^2 \end{pmatrix}. \tag{108}$$

We can formulate the two-term decomposition (104) because, as in the static case [8], we can segregate the n dependence of the $n > 1$ corrections in a transverse piece, leaving a longitudinal-hyperfine piece that has no n dependence. The resulting decomposition is not yet in Schmidt form, for the functions are not orthonormal, but we can easily transform it in Schmidt form. We begin by noting that

$$\langle \zeta_0 | \zeta_0 \rangle = 1, \tag{109}$$

$$\langle \zeta_0 | \zeta_1 \rangle = 0, \tag{110}$$

$$\langle \zeta_1 | \zeta_1 \rangle = \sum_{n=1}^{\infty} \frac{\langle \xi_n | \xi_0^3 \rangle^2}{(E_n - E_0)^2}, \tag{111}$$

$$\langle \vec{\varphi}_0 | \vec{\varphi}_0 \rangle = 1, \tag{112}$$

$$\langle \vec{\varphi}_0 | \vec{\varphi}_1 \rangle = \frac{1}{2} \left(\tilde{g}_{11} \eta_L^1 + \tilde{g}_{22} \eta_L^2 + 2 \tilde{g}_{12} \eta_L^{12} \right), \tag{113}$$

$$\langle \vec{\varphi}_1 | \vec{\varphi}_1 \rangle = \frac{1}{2} \left(\tilde{g}_{11}^2 \eta_{L6}^1 + \tilde{g}_{22}^2 \eta_{L6}^2 + (2\tilde{g}_{11} + \tilde{g}_{12}) \tilde{g}_{12} \eta_L^{112} + (2\tilde{g}_{22} + \tilde{g}_{12}) \tilde{g}_{12} \eta_L^{221} \right). \tag{114}$$

We now write

$$\vec{\psi}_{12} = \left(\zeta_0 + \epsilon \langle \vec{\varphi}_0 | \vec{\varphi}_1 \rangle \zeta_1 \right) \vec{\varphi}_0 + \epsilon \zeta_1 \left(\vec{\varphi}_1 - \langle \vec{\varphi}_0 | \vec{\varphi}_1 \rangle \vec{\varphi}_0 \right), \tag{115}$$

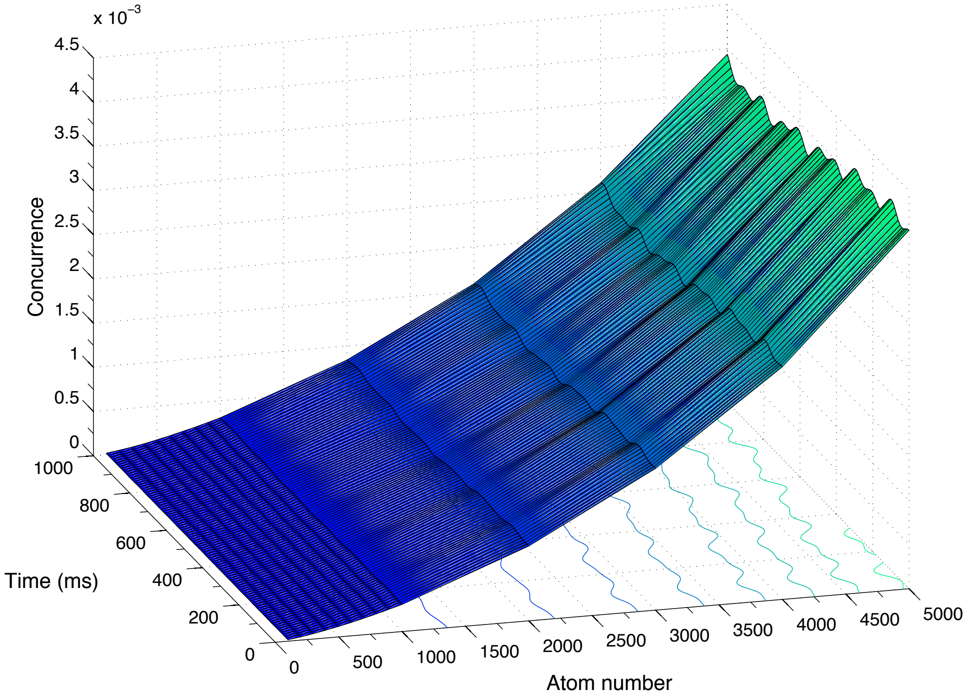

Figure 23. Concurrence (125) of the two-mode condensate state (120) as a function of time and atom number for $q = 2$. The entanglement remains remarkably small even for relatively large N, indicating that the condensate is well approximated by a single Schmidt term. In comparison to Figs. 24 and 25, the entanglement between the transverse dimensions and the longitudinal-hyperfine degrees of freedom decreases as the potential becomes more homogeneous.

which inspires us to define the following functions,

$$\chi_0 = \zeta_0 + \epsilon\langle\vec{\varphi}_0|\vec{\varphi}_1\rangle\zeta_1, \tag{116}$$

$$\chi_1 = \frac{\zeta_1}{\sqrt{\langle\zeta_1|\zeta_1\rangle}} \tag{117}$$

$$\vec{\phi}_0 = \vec{\varphi}_0, \tag{118}$$

$$\vec{\phi}_1 = \frac{\vec{\varphi}_1 - \langle\vec{\varphi}_0|\vec{\varphi}_1\rangle\vec{\varphi}_0}{\sqrt{\langle\vec{\varphi}_1|\vec{\varphi}_1\rangle - |\langle\vec{\varphi}_0|\vec{\varphi}_1\rangle|^2}}. \tag{119}$$

At the order we are working, χ_0 and χ_1 are orthonormal, whereas $\vec{\phi}_0$ and $\vec{\phi}_1$ are orthonormal by construction. Thus Eqs. (116)–(119) form the perturbative Schmidt basis of the two-mode condensate state (104). Therefore, we write

$$\vec{\psi}_{12} = \sqrt{\lambda_0}\chi_0\vec{\phi}_0 + \epsilon\sqrt{\lambda_1}\chi_1\vec{\phi}_1, \tag{120}$$

where the squared Schmidt coefficients are given by

$$\lambda_0 = 1, \tag{121}$$

$$\lambda_1 = \langle\zeta_1|\zeta_1\rangle\left(\langle\vec{\varphi}_1|\vec{\varphi}_1\rangle - |\langle\vec{\varphi}_0|\vec{\varphi}_1\rangle|^2\right). \tag{122}$$

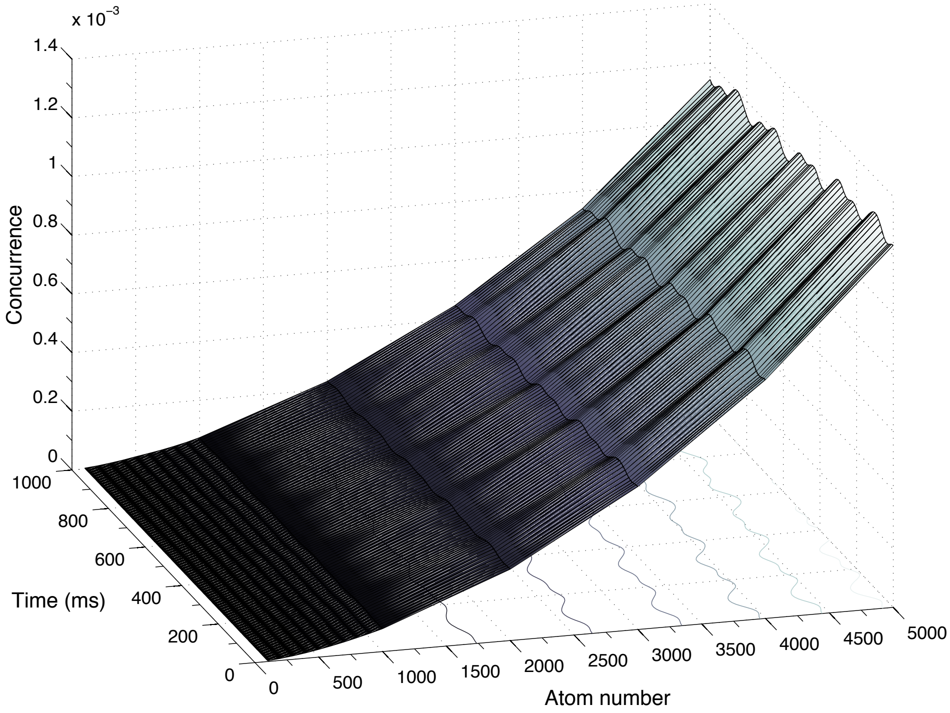

Figure 24. Concurrence (125) of the two-mode condensate state (120) as a function of time and atom number for $q = 4$. As for a harmonic trap, the entanglement between the transverse dimensions and the longitudinal-hyperfine degrees of freedom is remarkably small even for relatively large N, indicating that the condensate is well approximated by a single Schmidt term.

As in [8], we use Wootters's concurrence [24] to quantify the bipartite entanglement of state (104). The concurrence of a pure state of two qubits, $|\Psi_{AB}\rangle$, varies smoothly from 0 for product states to 1 for maximally entangled states. From its definition, $C = |\langle\Psi^*_{AB}|\sigma_y \otimes \sigma_y|\Psi^*_{AB}\rangle|$, in terms of the Pauli matrix σ_y and the complex conjugate of $|\Psi_{AB}\rangle$, it is easy to show that the concurrence for the perturbative condensate single-particle state (120) is given by

$$C = 2\sqrt{\lambda_0\lambda_1} = 2\langle\zeta_1|\zeta_1\rangle \left(\langle\vec{\varphi}_1|\vec{\varphi}_1\rangle - |\langle\vec{\varphi}_0|\vec{\varphi}_1\rangle|^2\right), \tag{123}$$

where we use the perturbative coefficients λ_0 and λ_1 as given by Eqs. (121) and (122).

In the case of a cigar-shaped BEC,

$$\langle\zeta_1|\zeta_1\rangle = \left(\frac{\eta_T}{2\hbar\omega_T}\right)^2 \mathrm{Li}_2(1/4), \tag{124}$$

where we use the polylogarithm function $\mathrm{Li}_s(z) \equiv \sum_{n=1}^{\infty} z^n/n^s$. Thus, it follows that

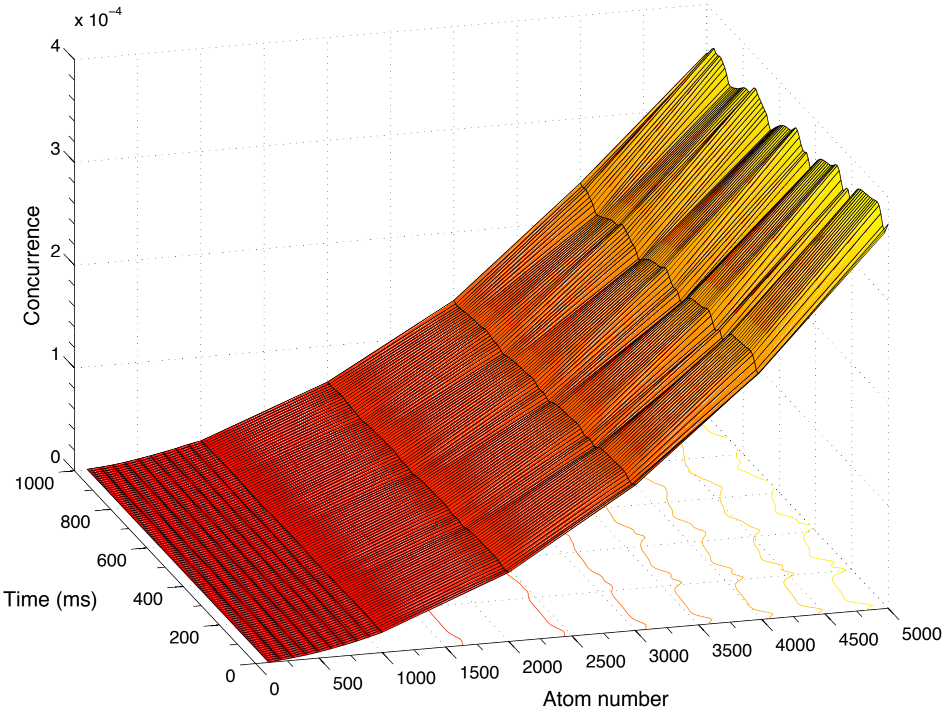

Figure 25. Concurrence (125) of the two-mode condensate state (120) as a function of time and atom number for $q = 10$. In comparison to the other traps, the concurrence for $q = 10$ has the lowest values. Therefore, to very good approximation the nonseparable corrections are indeed negligible.

the time-dependent concurrence can be written as

$$C = \left(\frac{\eta_T}{2\hbar\omega_T}\right)^2 \mathrm{Li}_2(1/4)\Bigg[\frac{\tilde{g}_{11}^2}{2}\Big(\eta_{L6}^1 - (\eta_L^1)^2\Big) + \frac{\tilde{g}_{22}^2}{2}\Big(\eta_{L6}^2 - (\eta_L^2)^2\Big) + \tilde{g}_{12}^2\Big(\eta_L^{112} + \eta_L^{221} - 2(\eta_L^{12})^2\Big) + \frac{1}{2}\big(\tilde{g}_{11}^2\eta_{L6}^1 + \tilde{g}_{22}^2\eta_{L6}^2 - 2\tilde{g}_{11}\tilde{g}_{22}\eta_L^1\eta_L^2\big) + 2\tilde{g}_{12}\big(\tilde{g}_{11}\eta_L^{112} + \tilde{g}_{22}\eta_L^{221} - \tilde{g}_{11}\eta_L^1\eta_L^{12} - \tilde{g}_{22}\eta_L^2\eta_L^{12}\big)\Bigg]. \tag{125}$$

We show the concurrence (125) in Figs. 23, 24, and 25 as a function of time and atom number, for $q = 2$, 4, and 10. In all cases, the concurrence oscillates in time as well as increases as N gets larger. More importantly, we can verify that the entanglement between the transverse and the remaining degrees of freedom is quite small for all cases, even for larger atom numbers. Moreover, it also decreases as the trap gets harder. These results indicate that the two-mode condensate state (120) is well described by the product state corresponding to the first Schmidt term. As we discussed before, the dominant term in the Schmidt decomposition corresponds to the optimal product-state approximation to state (100). This result not only confirms that the tightly confined dimensions can indeed be decoupled from the problem, but it naturally shows the optimal way to do it.

7. Conclusion

We have presented a detailed theoretical analysis of the mean-field dynamics and the reduced-dimension character of two-mode BECs in highly anisotropic traps. These systems are promising candidates for the implementation of high precision nonlinear interferometers and our analysis shows the feasibility of a recent experimental proposal of a Ramsey interferometry scheme [2].

In spite of the strong anisotropy of the condensate, our results also show that the effects of the nonlinear scattering interaction on the transverse degrees of freedom of the gas cannot be in general neglected. This brings into question the accuracy of the usual reduced-dimension (quasi-1D) approximation, both spatially and temporally. We have formulated a model that takes into account such 3D-induced effects by means of perturbative techniques. Because of the reshaping of the condensate in the transverse direction(s), additional effective three-body, attractive, intra- and inter-mode interactions have to be included in the reduced-dimension equations of the longitudinal dimension(s). Moreover, we have shown that these equations in fact provide the optimal reduced-dimension evolution for the two-mode condensate in general quasi-1D and quasi-2D geometries. We have demonstrated this result by developing a Schmidt decomposition of the two-mode condensate single-particle wave function, which separates out the transverse from the longitudinal-internal degrees of freedom. Using this formalism, we have verified that the entanglement between the transverse and the remaining degrees of freedom is quite small, even for larger atom numbers. In other words, this result shows that the two-mode condensate single-particle state is well described by the product state corresponding to the dominant term in the Schmidt decomposition. This corresponds to the optimal product-state approximation [22].

Finally, as far as the interferometry process goes, our perturbative model takes into account the spatial differentiation of the wave functions of the two modes and gives a significantly more accurate analytical account of the fringe signal than does the reduced-dimension approximation. We point out that this theoretical model is not limited to the study of interference effects, but can also be applied to the study of more general dynamics and different phenomena, such as soliton propagation.

Acknowledgments

We thank A. Shaji for discussions at the beginning of this project. This work was supported in part by National Science Foundation Grant Nos. PHY-0903953 and PHY-1005540.

References

[1] A. M. Rey, L. Jiang, and M. D. Lukin, Phys. Rev. A **76**, 053617 (2007).

[2] S. Boixo, A. Datta, M. J. Davis, S. T. Flammia, A. Shaji, and C. M. Caves, Phys. Rev. Lett. **101**, 040403 (2008).
[3] S. Choi and B. Sundaram, Phys. Rev. A **77**, 053613 (2008).
[4] S. Boixo, A. Datta, M. J. Davis, A. Shaji, A. B. Tacla, and C. M. Caves, Phys. Rev. A **80**, 032103 (2009).
[5] A. B. Tacla, S. Boixo, A. Datta, A. Shaji, and C. M. Caves, Phys. Rev. A **82**, 053636 (2010).
[6] A. B. Tacla, PhD Thesis, University of New Mexico (2012).
[7] V. Giovannetti, S. Lloyd, and L. Maccone, Phys. Rev. Lett. **96**, 010401 (2006).
[8] A. B. Tacla and C. M. Caves, Phys. Rev. A **84**, 053606 (2011).
[9] A. E. Muryshev, G. V. Shlyapnikov, W. Ertmer, K. Sengstock, and M. Lewenstein, Phys. Rev. Lett. **89**, 110401 (2002).
[10] S. Sinha, A. Y. Cherny, D. Kovrizhin, and J. Brand, Phys. Rev. Lett. **96**, 030406 (2006).
[11] L. Khaykovich and B. A. Malomed, Phys. Rev. A **74**, 023607 (2006).
[12] M. R. Matthews, D. S. Hall, D. S. Jin, J. R. Ensher, C. E. Wieman, E. A. Cornell, F. Dalfovo, C. Minniti, and S. Stringari, Phys. Rev. Lett. **81**, 243 (1998).
[13] D. S. Hall, M. R. Matthews, J. R. Ensher, C. E. Wieman, and E. A. Cornell, Phys. Rev. Lett. **81**, 1539 (1998).
[14] D. S. Hall, M. R. Matthews, J. R. Ensher, C. E. Wieman, and E. A. Cornell, Phys. Rev. Lett. **81**, 1543 (1998).
[15] K. M. Mertes, J. W. Merrill, R. Carretero-Gonzalez, D. J. Frantzeskakis, P. G. Kevrekidis, and D. S. Hall, Phys. Rev. Lett. **99**, 190402 (2007).
[16] R. P. Anderson, C. Ticknor, A. I. Sidorov, and B. V. Hall, Phys. Rev. A **80**, 023603 (2009).
[17] M. Egorov, R. P. Anderson, V. Ivannikov, B. Opanchuk, P. Drummond, B. V. Hall, and A. I. Sidorov, Phys. Rev. A **84**, 021605(R) (2011).
[18] M. Egorov, B. Opanchuk, P. Drummond, B. V. Hall, P. Hannaford, and A. I. Sidorov, arXiv:1204.1591 (2012).
[19] All numerical integrations are performed using the code generator *XmdS*, available at `www.xmds.org`, except for the integration of the time-independent, three-dimensional GP equation. For this integration we use the method described in C. M. Dion and E. Cancès, Comp. Phys. Comm. **177**, 787 (2007).
[20] In our simulations we assume that one can neglect the evolution of the spatial modes during the Ramsey pulses. According to [15, 16, 12], the two hyperfine levels of ^{87}Rb can be coupled by two-photon Rabi pulses whose duration is less than 1 ms, which is much faster than the characteristic time for the condensate to change its shape, thereby justifying such an approximation.
[21] Plots that are in harmonic trap units have (i) transverse (longitudinal) lengths in units of ρ_0 (z_0 for $q = 2$), (ii) transverse (longitudinal) marginal distributions in units of $1/\rho_0^2$ ($1/z_0$ for $q = 2$), and (iii) density in units of $1/(\rho_0^2 z_0)$.
[22] R. B. Lockhart and M. J. Steiner, Phys. Rev. A **65**, 022107 (2002).
[23] Nielsen M. and Chuang I., Quantum Computation and Quantum Information (Cambridge University Press, 2000).
[24] W. K. Wootters, Phys. Rev. Lett. **80**, 2245 (1998).